Improving sensitivity of trilinear R-parity violating SUSY searches using machine learning at the LHC

Arghya Choudhury[1,†] Arpita Mondal,[1,‡] Subhadeep Mondal,[2,§] and Subhadeep Sarkar[1,*]

[1]*Department of Physics, Indian Institute of Technology Patna, Bihar - 801106, India*
[2]*Department of Physics, SEAS, Bennett University, Greater Noida, Uttar Pradesh -201310, India*

In this work, we have explored the sensitivity of multilepton final states in probing the gaugino sector of a R-parity violating supersymmetric scenario with specific lepton number violating trilinear couplings (λ_{ijk}) being nonzero. The gaugino spectrum is such that the charged leptons in the final state can arise from the R-parity violating decays of the lightest supersymmetric particle (LSP) as well as R-parity conserving decays of the next-to-LSP (NLSP). Apart from a detailed cut-based analysis, we have also performed a machine learning-based analysis using a boosted decision tree algorithm, which provides much better sensitivity. In the scenarios with nonzero λ_{121} and/or λ_{122} couplings, the LSP pair in the final states decays to $4l\,(l = e, \mu) + E_T$ final states with a 100% branching ratio. We have shown that under this circumstance, a final state with $\geq 4l$ has the highest sensitivity while probing for gaugino masses. We also discuss how the sensitivity can change in the presence of τ lepton(s) in the final state due to other choices of trilinear couplings. We present our results through the estimation of the discovery and exclusion contours in the gaugino mass plane for both the high luminosity LHC (HL-LHC with $\sqrt{s} = 14$ TeV and $\mathcal{L} = 3000$ fb^{-1}) and high energy LHC (HE-LHC with $\sqrt{s} = 27$ TeV and $\mathcal{L} = 3000$ fb^{-1}). For the λ_{121} and/or λ_{122} nonzero scenario, the projected 2σ exclusion limit on NLSP masses reaches upto 2.37 TeV and 4 TeV for the HL-LHC and the HE-LHC, respectively, by using a machine learning based algorithm. We observe an enhancement of $\sim380\,(190)$ GeV in the projected 2σ exclusion limit on the NLSP masses at the 27 (14) TeV LHC. Considering the same final state ($N_l \geq 4$) for the λ_{133} and/or λ_{233} nonzero scenario, we find that the corresponding 2σ projected limits are ~1.97 TeV and ~3.25 TeV for the HL-LHC and HE-LHC, respectively.

I. INTRODUCTION

Supersymmetry (SUSY) [1–3] remains one of the most promising candidates for beyond the standard model (BSM) physics. This unique extension of the standard model (SM) can address some of the long-standing issues in particle physics, such as the hierarchy problem [4,5], the existence of dark matter (DM) [6–9], neutrino oscillation [10–16], *CP* violation [17–21], to name a few. One can also achieve gauge coupling unification [22–24] within this framework at a higher energy scale. However, no clear evidence of any SUSY particles has yet been obtained from the LHC or other particle physics experiments. This non-observation has led to bounds on these particles [25,26], subjected to the choice of model. The R-parity conserving (RPC) minimal supersymmetric standard model (MSSM) is the most widely studied scenario by the ATLAS and CMS Collaborations [25,26]. Apart from some small pockets of parameter space where the experimental sensitivities are not good enough, the existing LHC data can effectively rule out colored SUSY particle masses up to ~2.5 TeV [25–29]. The bounds are expectedly weaker in the electroweak sector, where the lower limits on the SUSY particle masses vary widely [30–38], depending on the particle spectrum and available decay modes. The RPC MSSM scenario has the added advantage of a natural DM candidate in the form of the lightest SUSY particle (LSP), but there is no theoretical reason why R-parity cannot be violated.

One of the direct consequences of R-parity violation (RPV) is either lepton number or baryon number violation by one unit. In principle, one can have both lepton number and baryon number violation together, but since that can give rise to proton decay, there are some stringent constraints on the choice of some of the RPV couplings [39].

*Corresponding author: subhadeep_1921ph21@iitp.ac.in
†arghya@iitp.ac.in
‡arpita_1921ph15@iitp.ac.in
§subhadeep.mondal@bennett.edu.in

In the presence of R-parity violation, the additional terms one can add in the superpotential are [39–41]

$$W_{\not{R}_p} = \mu_i H_u.L_i + \frac{1}{2}\lambda_{ijk}L_i.L_j e_k^c + \frac{1}{2}\lambda'_{ijk}L_i.Q_j d_k^c$$
$$+ \frac{1}{2}\lambda''_{ijk}u_i^c d_j^c d_k^c. \tag{1.1}$$

Here, L and Q represent left-handed lepton and quark superfields, respectively, and u, d, and e stand for right-handed up quark, down quark, and lepton superfields. H_u denotes an up-type Higgs superfield. i, j, k are generation indices, and c is charge conjugation. The first three terms in Eq. (1.1) violate the lepton number while the last term is responsible for baryon number violation. Unlike the RPC scenario, the LSP is no more stable, and it can decay into SM particles. Therefore, a collider signal of a RPC scenario is typically associated with larger missing energy as opposed to a RPV signal, which has a higher lepton/jet multiplicity. Depending on the choice of the LSP and nonzero RPV coupling, there can be a plethora of different kinds of final states [42–49]. The experimental collaborations have explored different possibilities to derive limits on the sparticle masses in the context of simplified RPV scenarios [50–61]. One of the major motivations to introduce a R-parity violation within SUSY framework is that it can explain neutrino oscillation data [62–73], which is one of the most robust indications of the existence of BSM physics. In addition to that, RPV SUSY has other advantages, e.g., one can obtain an additional contribution to a muon (g-2) [74–80] or explain flavor anomalies [81–84]. Refer to [40] for detailed phenomenological implications of various RPV SUSY scenarios.

As we wait for the LHC run-III to produce higher luminosity data, it is of utmost important to assess the impact of the existing data and gauge how much of the new physics parameter space can actually be probed at the highest possible luminosity. The gaugino sector of the MSSM is of particular interest because of various phenomenological implications. In the RPC context, the gaugino sector is vital in particular from the perspective of DM phenomenology [85–94] and muon (g-2) observation [77,87–89,95–108]. Hence, the collider phenomenology of various gaugino production and decay modes have been studied extensively [88,89,107–111]. A similar focus on the gaugino sector in the RPV context is somewhat lacking. There can be multiple final states depending on the NLSP-LSP mass gap and available RPV decay modes of the gauginos dictated by the nonzero RPV couplings and their relative strengths compared to the gauge couplings. The most stringent constraint on the neutralino-chargino mass plane in RPV context is provided by [112] through a four lepton final state. Looking at the structure of the λ_{ijk} coupling, there can be nine independent nonzero couplings. Depending on the chosen nonzero couplings, one can have

varied multiplicities of electrons, muons, and taus in the final state. The collider limits are not sensitive to flavors of the leptons as long as only electrons and muons are present in the final state. If we denote leptons as $l = e, \mu$, then the nine nonzero couplings lead to four different scenarios, and we have derived the limits on gaugino masses for all of them. Hence, in this study, we only concentrate on this multilepton final state arising from various production channels involving binolike neutralino LSP and winolike NLSP. While doing so, we assume that the RPV couplings are large enough such that the LSP decays are prompt. With the LHC running almost at full capacity, we need to look not only at the high luminosity option but possible higher center-of-mass (COM) energy options as well. The proposed extension of the COM energy to 27 TeV can be very effective in probing the SUSY scale further. It is necessary to assess what mass range one can effectively probe at this future collider to highlight its importance. LHC analyses are steadily moving towards machine learning with the accumulation of more and more data [113–117]. Algorithms like the gradient boosted decision tree (BDT) [118,119] can be adopted in collider studies in order to improve on the efficiency of traditional cut-based analyses depending on the suitable choice of kinematical variables. Improved sensitivity towards the new physics signal helps improve projected limits on new physics particle masses. For our analysis, we have adopted the BDT algorithm and used the XGBoost toolkit [120].

In Sec. II, we introduce our model framework and discuss the possible RPV decay modes of the bino LSP. We also discuss the various possible final state given the decay modes. In Sec. III, we briefly mention how the events are reconstructed. In Sec. III A, we define the signal regions for cut-based analysis for the HL-LHC. In this section, we also show the new projected exclusion limits on chargino and neutralino masses derived through our analysis. After that, we repeat the same final state analysis in the Sec. III B by using the machine learning (ML) algorithm and compare the results with that of cut-based analysis. In Sec. III C, we proceed with our analysis with 27 TeV COM energy in order to find the reach in chargino neutralino mass plane. We again do the ML-based analysis for 27 TeV COM energy and compare the results in Sec. III D. Finally, we conclude in Sec. IV.

II. MODEL FRAMEWORK

Among the different electroweakino productions, the wino production cross sections are the most significant ones. In this analysis, we consider a simplified RPV SUSY scenario with light winolike $\tilde{\chi}_1^{\pm}$ and $\tilde{\chi}_2^0$, which are mass degenerate. The LSP ($\tilde{\chi}_1^0$) is assumed to be pure binolike, and due to $\lambda_{ijk}L_iL_j\bar{E}_k$ coupling, it decays as $\tilde{\chi}_1^0 \rightarrow l_k'^{\pm} l_{i/j}'^{\mp} \nu_{j/i}$ via virtual sneutrino/sleptons, where $l' = e$, μ, and τ. We present all the possible decay modes of the

TABLE I. All possible decay modes of LSP $\tilde{\chi}_1^0$ (with 50% branching ratios each) corresponding to nine different coupling choices of λ_{ijk}, assuming only one coupling is nonzero.

	$k = 1$	$k = 2$	$k = 3$
$ij = 12$	$ee\nu_\mu, e\mu\nu_e$	$\mu e\nu_\mu, \mu\mu\nu_e$	$\tau e\nu_\mu, \tau\mu\nu_e$
$ij = 13$	$ee\nu_\tau, e\tau\nu_e$	$\mu e\nu_\tau, \mu\tau\nu_e$	$\tau e\nu_\tau, \tau\tau\nu_e$
$ij = 23$	$e\mu\nu_\tau, e\tau\nu_\mu$	$\mu\mu\nu_\tau, \mu\tau\nu_\mu$	$\tau\mu\nu_\tau, \tau\tau\nu_\mu$

LSP $\tilde{\chi}_1^0$ via $\lambda_{ijk}(i, j, k = 1, 2, 3)$ couplings in Table I for different allowed values of i, j, and k.[1] For a single nonvanishing coupling, $\tilde{\chi}_1^0$ decays to leptonic ($l = e/\mu$) final states with 100% branching ratios for λ_{121} and λ_{122}. On the other hand, λ_{133} and λ_{233} couplings allow the LSP to decay into tau enriched final states with 1τ and 2τ final states with 50% branching ratios each (see Table I). It may be noted that the generation wise branching ratio depends on the slepton mass with different flavors. However, in our analysis, we consider a mass degenerate slepton scenario (all three generations), as a result of which the generation wise branching ratios become equal with each other.

In the context of RPC SUSY searches, the most studied analysis is the $\tilde{\chi}_1^\pm\tilde{\chi}_2^0$ pair production with $3l + \rlap{/}{E}_T$ final states. But for RPV scenarios with LLE operators, signal efficiencies will depend on leptons coming from LSPs, rather than NLSPs ($\tilde{\chi}_1^\pm, \tilde{\chi}_2^0$). In this analysis, we consider $\tilde{\chi}_1^\pm\tilde{\chi}_2^0$ pair production along with $\tilde{\chi}_1^\pm\tilde{\chi}_1^\mp$ pair production.[2] Production cross section for the first process is roughly double of the later mode, and in both the cases, NLSPs dominantly produce via RPC couplings. It may be noted that $\tilde{\chi}_1^\pm\tilde{\chi}_1^\mp$, $\tilde{\chi}_1^0\tilde{\chi}_2^0$, $\tilde{\chi}_1^0\tilde{\chi}_1^0$, $\tilde{\chi}_2^0\tilde{\chi}_2^0$ production rates are almost vanishing for bino $\tilde{\chi}_1^0$ and winolike $\tilde{\chi}_1^\pm$ and $\tilde{\chi}_2^0$.[3] In our case, $\tilde{\chi}_1^\pm$ decays into $W^\pm\tilde{\chi}_1^0$, and $\tilde{\chi}_2^0$ can decay into $Z\tilde{\chi}_1^0$ and/or $h\tilde{\chi}_1^0$. For the sake of simplicity, we assume that $\mathrm{Br}(\tilde{\chi}_2^0 \to Z\tilde{\chi}_1^0) = \mathrm{Br}(\tilde{\chi}_2^0 \to h\tilde{\chi}_1^0) = 50\%$. From $\tilde{\chi}_1^\pm\tilde{\chi}_2^0$ and $\tilde{\chi}_1^\pm\tilde{\chi}_1^\pm$ pair productions, the final state always consists of a LSP pair and the lepton multiplicity in the final states depends on the choices of nonzero λ_{ijk}. In Table II, we summarize the charged lepton configuration coming from a LSP pair for only one single nonzero choice of λ_{ijk}.

TABLE II. Charged lepton configuration arises from a LSP pair in the RPV LLE scenarios for a single nonzero λ_{ijk} coupling. Four scenarios (*scenario-I* to *scenario-IV*) are defined according to the leptonic branching ratios for further analysis.

Nonzero couplings	Charged lepton configuration (branching ratios)			Remarks ($l = e, \mu$ only)
λ_{121}	$4e(25\%)$	$3e1\mu(50\%)$	$2e2\mu(25\%)$	$4l\ (100\%)$
λ_{122}	$4\mu(25\%)$	$3\mu1e(50\%)$	$2e2\mu(25\%)$	*scenario-I*
λ_{131}	$4e(25\%)$	$3e1\tau(50\%)$	$2e2\tau(25\%)$	$4l(25\%)$
λ_{232}	$4\mu(25\%)$	$3\mu1\tau(50\%)$	$2\mu2\tau(25\%)$	$3l1\tau(50\%)$
λ_{132}	$2\mu2e(25\%)$	$1e2\mu1\tau(50\%)$	$2\mu2\tau(25\%)$	$2l2\tau(25\%)$
λ_{231}	$2e2\mu(25\%)$	$2e1\mu1\tau(50\%)$	$2e2\tau(25\%)$	*scenario-II*
λ_{123}	$2e2\tau(25\%)$	$1e1\mu2\tau(50\%)$	$2\mu2\tau(25\%)$	$2l2\tau(100\%)$ *scenario-III*
λ_{133}	$2e2\tau(25\%)$	$1e3\tau(50\%)$	$4\tau(25\%)$	$2l2\tau(25\%)$
λ_{233}	$2\mu2\tau(25\%)$	$1\mu3\tau(50\%)$	$4\tau(25\%)$	$1l3\tau(50\%)$ $4\tau(25\%)$ *scenario-IV*

It is evident from Table II that if either λ_{121} or $\lambda_{122} \neq 0$, then the LSP pair gives $4l$ ($l = e, \mu$) $+ \rlap{/}{E}_T$ final states with 100% branching ratios (defined as scenario-I). It was shown in Ref. [121] that the mass limits are almost similar for $\lambda_{121} \neq 0$ and $\lambda_{122} \neq 0$ scenarios; i.e., the distinction between an electron and muon is not sensitive/essential in the $4l$ ($l = e, \mu$) $+ \rlap{/}{E}_T$ final states for obtaining the exclusion limits. It may be noted that when both λ_{121} and λ_{122} are nonzero, LSP decays via $e^\pm e^\mp\nu_\mu(25\%)$, $e^\pm\mu^\mp\nu_\mu(50\%)$, and $\mu^\pm\mu^\mp\nu_e(25\%)$, but the LSP pair contributes to $4l$ states similar to scenario-I. The other extreme case (scenario-IV) is obtained for $\lambda_{133} \neq 0$ or $\lambda_{233} \neq 0$, where tau enriched final states $2l2\tau(25\%)$, $1l3\tau(50\%)$, and $4\tau(25\%)$ emerge from the LSP pair. If both λ_{133} and λ_{233} are nonzero, then we also get the same final states. For other options of λ_{ijk}, the branching fractions of leptonic final states lie between these two extreme scenarios and are summarized in Table II. If both λ_{121} and $\lambda_{133} \neq 0$, then $\tilde{\chi}_1^0$ decay via $e^\pm e^\mp\nu_\mu, e^\pm\mu^\mp\nu_\mu$, $\tau^\pm e^\mp\nu_\tau$, and $\tau^\pm\tau^\mp\nu_e$ with each 25% branching fraction and eventually, the LSP pair leads to the final states: $4l(25\%)$, $3l1\tau(25\%)$, $2l2\tau(31.25\%)$, $1l3\tau(12.5\%)$, and $4\tau(6.25\%)$. Thus, the discovery reach/exclusion limits for scenarios with a combination of two or more nonzero λ_{ijk} will be achieved between *scenario-I* and *scenario-IV*.

III. COLLIDER ANALYSIS

For our analysis, we consider two production channels, $pp \to \tilde{\chi}_1^\pm\tilde{\chi}_2^0$ and $pp \to \tilde{\chi}_1^+\tilde{\chi}_1^-$. The Feynman diagram for these production channels and subsequent decays considered in this analysis are depicted in Fig. 1. As mentioned earlier, in the simplified model, the production and decays of NLSP occur via conventional RPC mode, and LSP decays promptly via RPV $LL\bar{E}$ couplings. Our focus will
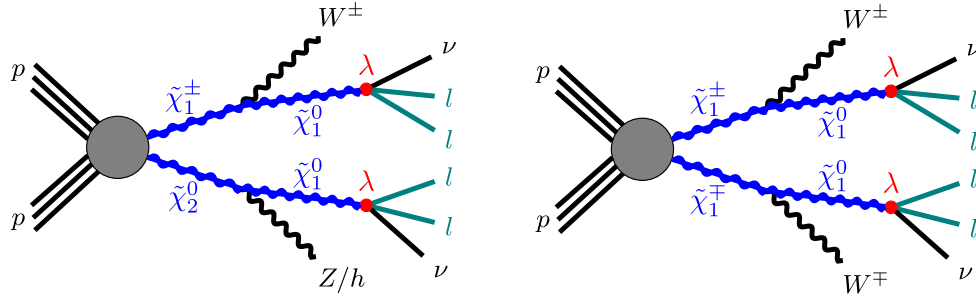
---

[1]Due to the gauge invariance of the superpotential, the couplings are antisymmetric in the first two indices, i.e., $\lambda_{ijk} = -\lambda_{jik}$.

[2]We keep the masses of the other SUSY particles likes squarks, gluino, sleptons, heavy Higgs bosons, and heavier electroweakinos fixed at beyond 5 TeV.

[3]For example, with the choice of input parameters, bino mass $M_1 = 100$ GeV, wino mass $M_2 = 1$ TeV, and Higgsino mass $\mu = 5$ TeV, $\sigma(pp \to \tilde{\chi}_1^\pm\tilde{\chi}_1^0)$ or $\sigma(pp \to \tilde{\chi}_2^0\tilde{\chi}_1^0)$, or $\sigma(pp \to \tilde{\chi}_2^0\tilde{\chi}_1^0)$ becomes $\sim 10^{-8}$ fb at 14 TeV LHC with decoupled squraks-gluino scenarios. With these same masses, one obtains $\sigma(pp \to \tilde{\chi}_1^\pm\tilde{\chi}_2^0) = 1.83$ fb, $\sigma(pp \to \tilde{\chi}_1^\pm\tilde{\chi}_1^\mp) = 0.84$ fb.

FIG. 1. Diagrams of winolike NLSP pair $\tilde{\chi}_1^\pm \tilde{\chi}_2^0$ and $\tilde{\chi}_1^\pm \tilde{\chi}_1^\mp$ productions via RPC electroweak process and the consequent decay of the LSP ($\tilde{\chi}_1^0$) via RPV $LL\bar{E}$ couplings.

be to obtain the sensitivity reach in the mass plane via detailed collider analysis in the scenario-I.[4] The leptons in the final state arise from the decay of the LSP as well as from the W/Z boson decay, which originates from the NLSP (illustrated in Fig. 1). Hence, we only consider the final states consisting of at least four leptons ($N_l \geq 4$, where $l = e, \mu$).

For the $N_l \geq 4$ channel, the most dominant source of backgrounds are $ZZ + $ jets, $WWZ + $ jets, and $t\bar{t}Z + $ jets. Additional contributions arise from $WZZ + $ jets, $ZZZ + $ jets, and Higgs (h) production via gluon gluon fusion (ggF). We have also generated/considered the processes like hjj, $Wh + $ jets, and $Zh + $ jets. In this analysis, we have not considered any reducible backgrounds like $t\bar{t}$, $Z + $ jets, $W + $ jets, WW etc., which may contain two/more fake or nonprompt leptons. In general, the irreducible backgrounds dominate for $N_l \geq 4$ channel. But the reducible background may dominate in the signal regions, where $m_{\rm eff}$ is relatively large and the uncertainty in the reducible background also dominates the total uncertainty [112]. The ATLAS Collaboration has derived the contribution of the reducible background from data using a faking efficiency and obtained that $t\bar{t}$ and $Z + $ jets contribute significantly in those signal regions. It may be noted that, to estimate the effect of reducible background on our result, we have calculated the exclusion reach by doubling, tripling, and quadrupling the value of our irreducible background. We have observed that effect of considering up to 3 times the original background is equivalent to the results obtained for 20% systematic uncertainty, and in later sections, we will present the exclusion reach considering 5% and 20% systematic uncertainty.

All the SM background events have been generated using MadGraph5-aMC@NLO [122] at the leading order (LO) parton level. The cross sections of different SM background processes used in this analysis and the generation level cuts have been tabulated/listed in Appendix A and Appendix C (see Tables XI and XIII for 14 TeV and

27 TeV COM energies, respectively). These events have been generated by matching up to two jets (for ZZ, three jets matched sample is used). The SUSY signal events have been generated using PYTHIA-6.4 [123]. The next-to-leading order + next-to-leading logarithmic (NLO + NLL) order cross sections have been computed for the signal events ($\tilde{\chi}_1^+ \tilde{\chi}_1^-$ and $\tilde{\chi}_1^\pm \tilde{\chi}_2^0$) by using Resummino-3.1.1 [124]. The showering and hadronization for background events have been done through -8, and for the signal events, we have used PYTHIA-6.4. Then all these events passed through a fast detector simulation in the DELPHES 3 platform [125] (version-3.5.0). Using anti-k_t algorithm [126], an algorithm within the FastJet [127] framework, jets have been reconstructed with jet radius parameter $R = 0.4$ along with transverse momentum $p_T > 20$ and pseudorapidity range $|\eta| < 2.8$. Following the ATLAS analysis [112], the b-tagging efficiency has been chosen to be 85% and the light jet mistagging efficiency (as b-jet) 25%. For the identification of b-jets, the pseudorapidity range $|\eta| < 2.5$ has been considered.

For the reconstruction of leptons (electron, muon), we have followed the isolation, overlap removal procedures etc. according to the ATLAS analysis as mentioned in Sec. 5 of [112]. The final state electrons (muons) are required to have $p_T > 7 \, (5)$ GeV, $|\eta| < 2.47 \, (2.7)$, and must satisfy both the track isolation and calorimeter isolation criteria. We have considered the Loose isolation criteria [128,129] for both the leptons where the conditions on the scalar sum of p_T of the surrounding particles are $\sum p_T^{\rm varcone20}/p_T^{e(\mu)} < 0.15 \, (0.15)$ and $\sum E_T^{\rm cone20}/p_T^{e(\mu)} < 0.20 \, (0.30)$ for tracker and calorimeter isolation, respectively, for selected electrons (muons).[5] Furthermore, in order to ensure that charged leptons arising from the decays of low mass particles while showering do not contaminate

---

[4]We also discuss about the exclusion reach of our signals in other scenarios mentioned in Table II.

[5]Surrounding objects with $p_T \geq 1.0$ GeV are chosen within a cone radius of $\Delta R = 0.2$ of leptons for calorimeter isolation. For track isolation, a variable cone of $\min[10 \, {\rm GeV}/p_T^e, 0.2]$ and $\min[10 \, {\rm GeV}/p_T^\mu, 0.3]$ are considered for electron and muon, respectively. ΔR is calculated from the differences of pseudorapidity and azimuthal angle as $\Delta R = \sqrt{(\Delta\eta)^2 + (\Delta\phi)^2}$.

our signal regions, both leptons are discarded if they form an opposite sign (OS) or a same flavor opposite sign (SFOS) pair with the invariant mass of the pair being $M_{OS} < 4$ GeV and $8.4 < M_{SFOS} < 10.4$ GeV, respectively. In the next subsections (Sec. III A and Sec. III B), we will first present a detailed cut based collider study for the HL-LHC, and then we will study the improvement on the exclusion reach by using machine learning-based methods. In a similar manner, the future prospects for the HE-LHC will be presented in Sec. III C and Sec. III D.

A. Prospect at the HL-LHC using cut-based analysis

In this section, we present the search prospect of wino pair production at the High Luminosity LHC (HL-LHC) with $N_l \geq 4$ channel at center-of-mass energy, $\sqrt{s} = 14$ TeV and luminosity, $\mathcal{L} = 3000$ fb^{-1} via a traditional cut-and-count analysis. Using the run-II LHC data, the ATLAS Collaboration has already excluded wino mass around 1.5 TeV [112] for relatively large $m_{\tilde{\chi}_1^0}$, and for the cut-based analysis, we closely follow this analysis. We validate our simulation setup by comparing our results to that obtained by the ATLAS Collaboration [112]. The comparison is presented in the form of a cut-flow table and an exclusion plot in Appendix D. We carry our analysis for two signal regions: SR-A and SR-B,[6] which are optimized for smaller and larger masses of $\tilde{\chi}_1^\pm / \tilde{\chi}_2^0$, respectively. For these signal regions, we estimated the signal yields by varying the $m_{\tilde{\chi}_1^\pm}(= m_{\tilde{\chi}_2^0})$ in the range 1–3 TeV and $m_{\tilde{\chi}_1^0}$ in the range 50 GeV to $(m_{\tilde{\chi}_2^0}-10)$ GeV[7] with a step size of 10 GeV. We have chosen three signal benchmark points to showcase our results—BP1: $m_{\tilde{\chi}_1^\pm} = 1600$ GeV, $m_{\tilde{\chi}_1^0} = 250$ GeV, BP2: $m_{\tilde{\chi}_1^\pm} = 1800$ GeV, $m_{\tilde{\chi}_1^0} = 800$ GeV, BP3: $m_{\tilde{\chi}_1^\pm} = 1950$ GeV, $m_{\tilde{\chi}_1^0} = 1850$ GeV. These benchmark points are selected on the basis of mass difference between $m_{\tilde{\chi}_1^\pm}$ and $m_{\tilde{\chi}_1^0}$ i.e., large, intermediate and small mass differences. The details of the background cross section along with the yield after the generation level cut are summarized in Table XI and the NLO + NLL level cross sections for the benchmark points have been tabulated in Table XII.

As mentioned earlier, $ZZ +$ jets, $WWZ +$ jets, and $t\bar{t}Z +$ jets are the most dominant backgrounds. We present the transverse momentum distribution of the leading lepton $(p_T^{l_1})$ of these dominant SM background channels along with signal corresponding to the three chosen benchmark points in Fig. 2. The blue, green, and magenta color solid lines represent the distributions corresponding to the $ZZ +$ jets, $t\bar{t}Z +$ jets, and $WWZ +$ jets background

FIG. 2. Distributions of transverse momentum of leading lepton $(p_T^{l_1})$ at the HL-LHC ($\sqrt{s} = 14$ TeV with $\mathcal{L} = 3000$ fb^{-1}) are shown here. The blue, green, and magenta color solid lines represent the most dominant $ZZ +$ jets, $t\bar{t}Z +$ jets and $WWZ +$ jets backgrounds. Yellow, cyan, and red filled regions correspond to the benchmark points—BP1, BP2, and BP3, respectively.

channels, respectively. The same for the benchmark points—BP1, BP2, and BP3 are shown in yellow, cyan, and red filled regions, respectively. It is evident from the Fig. 2 that for all the SM backgrounds the leading lepton p_T peak occurs at a lower value compared to that for signals. Also, among the benchmark points, BP3 has the largest $m_{\tilde{\chi}_1^0}$, which leads to a shift of the peak to the higher value of p_T compared to BP1 and BP2. For both the signal regions (SR-A and SR-B), we choose a cut $p_T^{l_1} > 100$ GeV, which will effectively discard the events coming from the SM backgrounds. To save computation time, therefore, $p_T^{l_1} > 100$ GeV cut is applied for all the background channels at the generation level itself. We have summarized the yield of background events after applying this generation level cuts in the last column of Table XI in Appendix-A. This cut

FIG. 3. Distributions of effective mass (m_{eff}) at the HL-LHC ($\sqrt{s} = 14$ TeV, $\mathcal{L} = 3000$ fb^{-1}) are shown here. Color conventions are same as in Fig. 2.

---

[6]The signal regions are differentiated through a different $m_{\text{eff}} = \sum_i p_T^{l_i} + \sum_i p_T^{j_i} + E_T$ cut as discussed later.
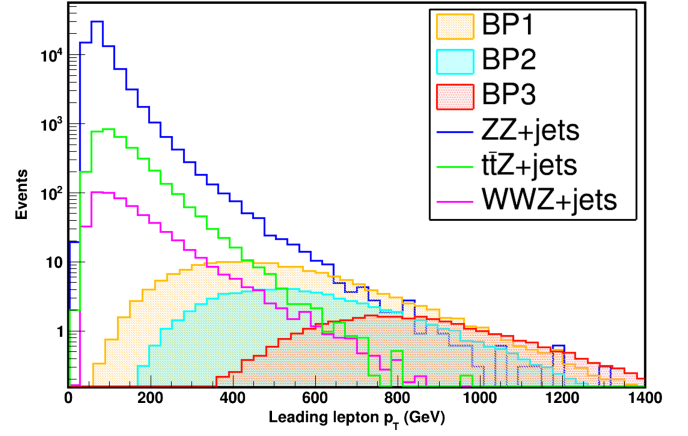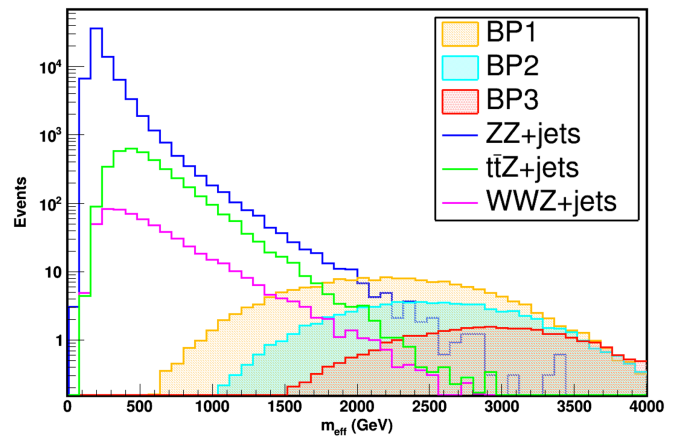[7]To assure the prompt decay of $\tilde{\chi}_1^0$.

TABLE III. Selection cuts and the corresponding yields for the three signal benchmark points and relevant background channels at the HL-LHC are shown here. Statistical signal significance (σ_{ss}) without any systematic uncertainty for BP1, BP2, and BP3 are also shown. Corresponding signal significance σ_{ss}^ϵ with sys. unc. $\epsilon = 5\%$ are presented in parenthesis. Here, the SUSY signals belong to scenario-I.

Cut variables	$N_l \geq 4$ ($l = e, \mu$) + $p_T^{l_1} > 100$ GeV	Z veto	b veto	Signal region	
				SR-A ($m_{\rm eff} > 900$)	SR-B ($m_{\rm eff} > 1500$)
BP1	172.35	145.98	96.22	94.74	81.35
BP2	74.68	70.61	46.34	46.25	43.76
BP3	32.42	30.83	19.56	19.55	19.29
ZZ + jets	17350	126.56	115.63	5.79	1.12
$t\bar{t}Z$ + jets	2320	183.21	43.25	5.25	0.73
WWZ + jets	378.77	29	25.67	6.32	1.33
WZZ + jets	217.78	3.83	3.19	0.71	0.13
ZZZ + jets	104.76	1.02	0.78	0.07	0.01
h via GGF	1660	14.48	12.98	1.31	0.15
hjj	66.84	17.7	14.63	0.51	0.011
Wh + jets	16.09	4.86	4.14	0.15	0.01
Zh + jets	9.93	2.16	1.65	0.08	0.007
	Total background			20.19	3.498
Signal significance σ_{ss} (σ_{ss}^ϵ, sys. unc. = 5%)			BP1	8.84 (7.79)	8.83 (8.02)
			BP2	5.67 (5.25)	6.36 (6.02)
			BP3	3.10 (2.96)	4.04 (3.93)

reduces the most dominant ZZ + jets background contribution by a factor of ~ 5, whereas the signal events for benchmark points almost remain the same (reduced by only 1%–2%).

Among the relevant kinematic observables, $m_{\rm eff} = \sum_i p_T^{l_i} + \sum_i p_T^{j_i} + \not{E}_T$ turns out to be the most effective one. We observe that the maximum signal significance is obtained by optimizing the $m_{\rm eff}$ variable along with Z veto[8] and a b-jet veto on the $N_l \geq 4$ final states. The $m_{\rm eff}$ distributions for signal benchmark points and dominant backgrounds are depicted in Fig. 3, where we have followed the same color conventions to represent signal benchmark points and background channels as Fig. 2. Similar to Fig. 2, the $m_{\rm eff}$ distributions for SM background channels peak at much lower values compared to SUSY signals. The distributions corresponding to the signal benchmark points also differ depending on the choices of LSP and NLSP masses. Consequently, two signal regions are defined; SR-A and SR-B with $m_{\rm eff} > 900$ GeV and $m_{\rm eff} > 1500$ GeV, respectively. The $m_{\rm eff}$ cut reduces the number of background events significantly. Apart from this, the Z-veto cut is most effective to reduce the ZZ + jets events while b-veto is very effective to reduce $t\bar{t}Z$ + jets events.

Finally, we estimate the statistical signal significance (σ_{ss}) using the relation $\sigma_{ss} = S/\sqrt{S + B}$, where S and B represent the signal and background yield. The effects of systematic uncertainties are also shown by considering the formula $\sigma_{ss}^\epsilon = S/\sqrt{S + B + ((S + B)\epsilon)^2}$, where ϵ corresponds to the systematic uncertainty (sys. unc.). The list of selection cuts used for this cut-and-count analysis along with the yield of signal benchmark points and the SM backgrounds after each cut for the HL-LHC are tabulated in Table III. The signal significance σ_{ss} without any systematic uncertainty for BP1, BP2, and BP3 are also shown in the last three rows of Table III. We obtain that σ_{ss} for BP1, BP2, and BP3 are 8.84 (8.83), 5.67(6.36), and 3.1(4.04), respectively, for the signal region SR-A (SR-B). SR-B consists of larger $m_{\rm eff}$ criteria compared to SR-A and is more effective to probe the parameter space with large $m_{\tilde{\chi}_1^\pm}$ as evident in Table III. We also present the signal significance σ_{ss}^ϵ with systematic uncertainty $\epsilon = 5\%$ for the benchmark points in Table III. For BP1, BP2, and BP3, the signal to background ratio (S/B) is ~ 23, 12, 5, respectively, for SR-B[9] and the changes in σ_{ss} for including the systematic uncertainty is not significant due to this large S/B ratio. We find that $\epsilon = 5\%$ reduces the σ_{ss} by 3%–12%.

---

[8]Invariant mass of same-flavor-opposite-sign charged lepton pairs has to fall outside the window $101.2 \geq m_{ll} \geq 81.2$ GeV.

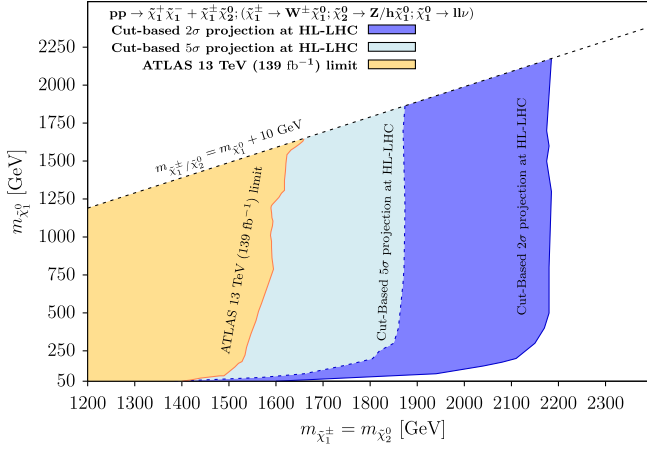[9]For SR-A, the corresponding ratio is ~ 5, 2, 1, respectively.

FIG. 4. Projected discovery (5σ) and exclusion (2σ) regions in the $m_{\tilde{\chi}_2^0} - m_{\tilde{\chi}_1^0}$ mass plane at the HL-LHC are presented with light and dark blue colors. The yellow region represents the existing limit obtained by the ATLAS Collaboration from run-II data [112].

In Fig. 4, we showcase the projected discovery region (with $\sigma_{ss} \geq 5$) and exclusion region (with $\sigma_{ss} \geq 2$) in the LSP-NLSP mass plane from direct $\tilde{\chi}_1^{\pm}\tilde{\chi}_2^0 + \tilde{\chi}_1^+\tilde{\chi}_1^-$ production for scenario-I at the HL-LHC. The projected 5σ discovery and 2σ exclusion regions obtained by traditional cut-and-count analysis are represented by the boundaries of light and dark blue colored regions, respectively. The yellow region corresponds to the current 95% C.L. observed limit obtained by the ATLAS Collaboration using run-II (13 TeV) 139 fb^{-1} data [112]. The black dashed line in Fig. 4 represents the NLSP-LSP mass relation $m_{\tilde{\chi}_2^0} - m_{\tilde{\chi}_1^0} = 10$ GeV. It is evident that HL-LHC is capable of extending the 5σ projected discovery reach by around 200 GeV compared to the current LHC limit. Using this traditional cut-based analysis, we also observe that the 95% C.L. projected exclusion limits

on $m_{\tilde{\chi}_2^0} = m_{\tilde{\chi}_1^{\pm}}$ reaches up to 2100 (2180) GeV at the HL-LHC for $m_{\tilde{\chi}_1^0} > 200$ (500) GeV.

We have defined four different scenarios (scenario-I,II,III,IV) in Sec. II (see Table II) obtained from different single nonzero λ_{ijk} couplings. The LSP pair gives $4l(l = e, \mu) + \not{E}_T$ final states with 100% branching ratios in scenario-I. In this section, we have already discussed the prospect of scenario-I for various benchmark points along with the projected exclusion in mass planes in great detail. For other scenarios, τ lepton appears in the final state with scenario-IV being the most τ enriched.

It may be noted that using the run-II data, the ATLAS Collaboration has explored the scenario-IV using dedicated tau tagging analysis [112] and excluded $m_{\tilde{\chi}_1^{\pm}}$ up to ~1.1 TeV in the tau enriched scenario-IV [112]. The limit obtained by the dedicated tau channel in scenario-IV is weaker by ~470–480 GeV compared to the limit obtained by the $4l$ channel (~1.58 TeV) in scenario-I. But we have checked that the $4l$ channel gives comparable reach as tau tagged analysis in scenario-IV. The gain in the production cross section is compensated by the reduction in signal efficiencies and leads to a comparable exclusion limit.

Now we proceed to explore the prospect of our conventional cut based $4l(l = e, \mu)$ analysis for these other scenarios considering the already selected signal benchmark points. We present the signal significance of BP1, BP2, and BP3 for the four scenarios in Table IV without and with a systematic uncertainty of $\epsilon = 5\%$. As expected, the σ_{ss} is maximum for scenario-I and minimum for scenario-IV owing to the comparatively lower leptonic branching ratios for τ enriched final states. As Fig. 4 shows, the exclusion limits on $m_{\tilde{\chi}_1^{\pm}}$ are almost constant for a relatively larger $m_{\tilde{\chi}_1^0}$; we also estimate the projected exclusion limits on $m_{\tilde{\chi}_1^{\pm}}$ at the HL-LHC for the four models by fixing the LSP mass at 800 GeV (same with BP2). We derive that for this specific choice of $m_{\tilde{\chi}_1^0}$, the projected 2σ

TABLE IV. Comparison of signal significance of benchmark points BP1, BP2, and BP3 for different model scenarios (defined in Table II) with 0% (5%) systematic uncertainty are shown here. The numbers in last row represents the projected 95% C.L. 2σ exclusion limits on NLSP masses for a fixed 800 GeV LSP with 0% (20%) systematic uncertainty. Here, all the masses are in GeV.

Benchmark points	Signal significance (sys. unc. = 5%)			
	Scenario-I	Scenario-II	Scenario-III	Scenario-IV
BP1	8.83 (8.02)	6.46 (6.10)	3.64 (3.56)	2.33 (2.30)
BP2	6.36 (6.02)	4.67 (4.51)	2.75 (2.70)	1.69 (1.67)
BP3	4.04 (3.93)	2.93 (2.88)	1.66 (1.64)	0.92 (0.91)
$m_{\tilde{\chi}_1^0}$	Projected exclusion on $m_{\tilde{\chi}_1^{\pm}}$ at the HL-LHC (sys. unc = 20%)			
800	2180 (2120)	2080 (2020)	1900 (1840)	1740 (1680)

exclusion limits on $m_{\tilde{\chi}_1^\pm}(=m_{\tilde{\chi}_2^0})$ become 2.18, 2.08, 1.90, and 1.74 TeV for `scenario-I`, `scenario-II`, `scenario-III`, and `scenario-IV`, respectively. Thus, the exclusion reach on $m_{\tilde{\chi}_1^\pm}(=m_{\tilde{\chi}_2^0})$ is weaker by $\sim$440 GeV for `scenario-IV` as compared to `scenario-I`. It is also observed that the mass limits gets reduced by $\sim$60 GeV for systematic uncertainty $\epsilon = 20\%$ (refer to the last row in Table IV).

B. Prospect at the HL-LHC using machine learning based analysis

We now proceed to use a boosted decision tree (`BDT`) based machine learning algorithm to assess if the results of our cut-based analysis can be improved upon. For this purpose, we construct the following set of 18 kinematical variables (also called "features" in ML language), taking into account the kinematics of the multilepton final state.

  (i) Transverse momenta of leading lepton ($p_T^{l_1}$) and subleading lepton ($p_T^{l_2}$)[10] (two variables)
  (ii) ΔR ($\Delta R = \sqrt{(\Delta\eta)^2 + (\Delta\phi)^2}$, where η is pseudorapidity and ϕ is azimuthal angle) between leading lepton and other subleading leptons, denoted as $\Delta R_{l_1 l_2}$, $\Delta R_{l_1 l_3}$, $\Delta R_{l_1 l_4}$; and similarly, ΔR between other leptons, $\Delta R_{l_2 l_3}$, $\Delta R_{l_2 l_4}$, and $\Delta R_{l_3 l_4}$ (six variables)
  (iii) Difference in azimuthal angle between leptons and missing transverse momenta, which are $\Delta\phi_{l_1 \not{E}_T}$, $\Delta\phi_{l_2 \not{E}_T}$, $\Delta\phi_{l_3 \not{E}_T}$, and $\Delta\phi_{l_4 \not{E}_T}$ (four variables)
  (iv) Number of jets at each event, both b-tagged jets (N_b) and non b-tagged jets (N_j) (two variables)
  (v) Missing transverse energy ($\not{E}_T$) and effective mass (m_{eff}) as defined in Sec. III A (two variables)
  (vi) Number of same flavor opposite sign lepton pair (N_{SFOS}) and number of SFOS pair lies within the range $81.2 \leq m_{\text{SFOS}} \leq 101.2$ GeV (N_Z) (two variables)

For our ML-based multivariate analysis, we have used extreme gradient boosted decision tree algorithm through XGBoost machine learning toolkit [120]. Training and testing of the XGBoost module are done by implementing the multiclass classification through `multi:softprob` objective function. The SUSY signal events and the SM backgrounds events, which contain at least $4l(l = e, \mu)$, are only considered.[11] Details of lepton and jets identification, isolation criteria etc. are already summarized in Sec. III A. After calculating the 18 kinematic observables, the signal and background events are mixed with proper weight

according to their relative cross sections. We have used 80% of this dataset for training and the remaining for testing. The hyperparameters `learning rate`, `number of trees`, `maximum depth` are tuned to optimize the signal significance. The `number of trees` and `maximum depth` of a tree are chosen as 500 and 10, respectively. The `learning rate` (η) parameter or step size shrinkage is chosen in the range [0.01–0.03] to prevent overfitting. The η parameter shrinks the features weights at each boosting step, which makes the process more conservative [130]. The `multi:softprob` objective function returns the predicted probability score of each data point belonging to each class (signal and multiple backgrounds). To obtain the discovery and exclusion contours on the gaugino mass plane, we have applied a threshold on the probability score to obtain maximum significance. It may be noted that additional statistical uncertainty can arise from the ML analysis. To estimate any statistical uncertainty arising from our ML analysis, we have (a) shuffled our data files randomly and ran the same ML analysis on them multiple times to check how much the results differ and (b) varied the hyperparameters used in the ML analysis to check their effect on the final result. We observe that for our analysis, despite some small fluctuations in total background yield for different random orientation of the signal and background events in the data file and/or with different learning rates, the variation in signal significance remains reasonably small.

All the kinematic variables or the "features" are not equally effective in predicting the signal and different background classes. To understand the effect of each feature in predicting each class distinctly, we computed Shapley values using Shapley additive ex-planations (SHAP) [131,132] package. In collider studies, SHAP values are very helpful to understand the effect of each feature on the model's output [113,118,133,134]. To find out the average marginal contribution of a feature, SHAP finds out the difference between the two outputs of model prediction by training the model with the feature and also excluding the same feature. Then it calculates the weighted average of the possible differences for different subsets of all features [133]. In this way, the global feature importance is calculated for every feature, and furthermore, the SHAP value of each feature for every event and the mean of absolute Shapley values are calculated by averaging over all the events. According to the mean of the absolute values, SHAP ranks the features and the feature importance plot for the top ten kinematic variables for the benchmark SUSY signal BP2 ($m_{\tilde{\chi}_1^\pm} = 1800$, $m_{\tilde{\chi}_1^0} = 800$) and various backgrounds is displayed in the left panel of Fig. 5. We observe that N_Z has the most significant effect on predicting the signal and backgrounds for BP2 and the next five important features are m_{eff}, $\not{E}_T$, $p_T^{l_2}$, N_b, and $p_T^{l_1}$. For the cut-based analysis, we also find that these variables are effective to discriminate the SUSY signal and backgrounds (refer to

---

[10]The ordering of leptons are based on their transverse momenta, l_1 denotes the lepton with highest p_T at each event, l_2 denotes the lepton with second highest p_T value at that event and so on.

[11]No generation level p_T cuts are applied for the signal/background events.
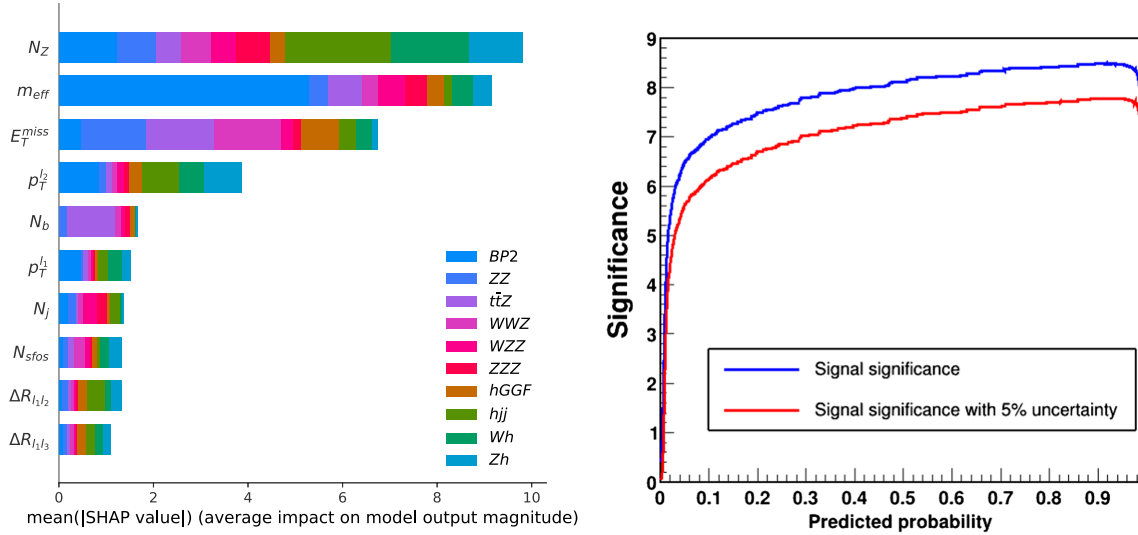
FIG. 5.   (Left) Shapley feature importance plot for the top ten important kinematic variables for the dataset with benchmark SUSY signal BP2 ($m_{\tilde{\chi}_1^\pm} = 1800$, $m_{\tilde{\chi}_{1_L}^0} = 800$) and backgrounds analyzed at HL-LHC. (Right) The signal significance without any systematic uncertainty (blue line) and with 5% systematic uncertainty (red line) as a function of predicted probability are shown.

Figs. 2–3 for $p_T^{l_1}$ and m_{eff} distribution, Table III for cut flow, and for more details, refer to Sec. III A). In Fig. 5 (left), the spread of the color bar along x axis corresponds to the contribution of that feature to classify that particular class.

In the right panel of Fig. 5, we present the variation of signal significance as a function of probability score cut. The blue line corresponds to σ_{ss}^ϵ with systematic uncertainty $\epsilon = 0\%$, and the red line represents the same with $\epsilon = 5\%$. It is evident that the signal significance reaches a maximum and saturates around probability score ∼0.90–0.95. We present the signal yield, total background yield, and the signal significance (without any systematic uncertainty) at the HL-LHC in the Table V for two sample values of probability score cut 0.90 and 0.96 chosen from the saturated region. Comparing the signal significance obtained via the traditional cut-and-count method (refer to

Table III), we observe that roughly ∼30%–40% gain is achieved for ML-based analysis. Numbers in the parenthesis correspond to σ_{ss} and gain with systematic uncertainty $\epsilon = 5\%$. It may be noted that similar to Table III, here the SUSY signal belongs to scenario-I. For this same scenario, we also estimate the projected 5σ discovery reach and 2σ exclusion regions in the $m_{\tilde{\chi}_2^0} - m_{\tilde{\chi}_1^0}$ mass plane at the HL-LHC in Fig. 6, represented by light and dark violet color, respectively. The light and dark blue regions correspond to projected 5σ and 2σ regions obtained from the conventional cut-and-count method. Similar to Fig. 4, the yellow regions are already ruled out by the ATLAS 13 TeV data [112].

As evident from Table V, the ML-based analysis improves the sensitivity by ∼30%–40% due to its superior capability of segregating signal from various background

TABLE V.   Signal yield, total background yield and the signal significance (without any systematic uncertainty) at the HL-LHC using ML-based algorithm for different probability scores are presented here. The numbers in the parenthesis correspond to σ_{ss} with systematic uncertainty $\epsilon = 5\%$. Here, the SUSY signal belongs to scenario-I.

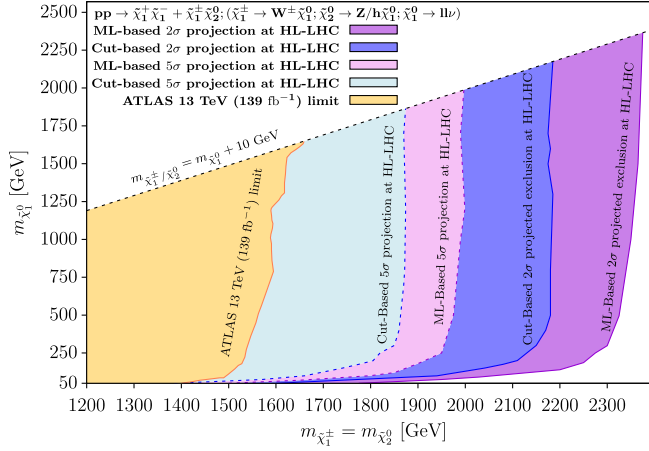| Benchmark points	Probability score	Signal yield	Total background yield	Signal significance σ_{ss} (sys. unc = 5%)	Gain in σ_{ss} from cut based
BP1	0.90	165.80	6.99	12.61 (10.54)	43% (31%)
	0.96	156.89	3.94	12.37 (10.45)	40% (30%)
BP2	0.90	73.84	1.96	8.48 (7.78)	33% (29%)
	0.96	72.47	1.34	8.44 (7.75)	33% (29%)
BP3	0.90	32.32	1.32	5.57 (5.35)	38% (36%)
	0.96	31.97	0.30	5.63 (5.41)	40% (38%)

FIG. 6. Projected discovery (5σ) and exclusion (2σ) reach in the $m_{\tilde{\chi}_2^0} - m_{\tilde{\chi}_1^0}$ mass plane at the HL-LHC are presented with light and dark violet colors. For the light blue, dark blue, and yellow color, the color conventions are same as in Fig. 4. The yellow regions represents the existing limit obtained by the ATLAS Collaboration from run-II data [112].

channels. This leads to a greater reach for discovery and exclusion in the bino-wino mass plane (Fig. 6). The projected discovery reach extends to ~1.99 TeV in ML-based methods with an enhancement of 120 GeV compare to the cut-based method. Similarly, the projected exclusion curve reaches ~2.37 TeV from our cut-based estimate of ~2.18 TeV (enhancement of 190 GeV). In Table VI, we have presented the signal significance corresponding to different benchmark points for each SUSY scenario (as defined in Table II). Similar to cut-based analysis, the σ_{ss} is maximum for scenario-I and minimum for the scenario-IV. We have also shown the projected exclusion limit found for each scenario at the LSP mass 800 GeV without and with 20% systematic uncertainty. As similar to σ_{ss}, the 2σ reach is also maximum for scenario-I (2340 GeV) and minimum for scenario-IV (1935 GeV) and the gap between the two

2σ reaches corresponding to without and with 20% systematic uncertainty is around 65 GeV for each scenario. It may be noted that the projected exclusion limits on $m_{\tilde{\chi}_1^\pm}$ as mentioned in Table VI improve by ~30 GeV if the LSP-NLSP mass gap is ~10 GeV.

C. Prospect at the HE-LHC using cut-based analysis

In this section, we present the cut-and-count analysis for the search of wino pair production at the High Energy LHC (HE-LHC) with $N_l \geq 4$ final state at $\sqrt{s} = 27$ TeV and $\mathcal{L} = 3000$ fb^{-1} as presented in Sec. III A for HL-LHC. For this analysis, we have defined two signal regions as SR-C and SR-D with $m_{\mathrm{eff}} > 1500$ GeV and $m_{\mathrm{eff}} > 2200$ GeV, respectively, along with other cuts like $p_T^{l_1} > 150$ GeV, Z-veto and b-veto. We have defined three representative signal benchmark points—BP4: $m_{\tilde{\chi}_1^\pm} = 2300$ GeV, $m_{\tilde{\chi}_1^0} = 250$ GeV, BP5: $m_{\tilde{\chi}_1^\pm} = 2900$ GeV, $m_{\tilde{\chi}_1^0} = 1200$ GeV, BP6: $m_{\tilde{\chi}_1^\pm} = 3100$ GeV, $m_{\tilde{\chi}_1^0} = 3000$ GeV. The cross sections of wino pair production corresponding to these benchmark points at NLO + NLL level are mentioned in Table XII in Appendix-B.

The transverse momentum distribution of the leading lepton ($p_T^{l_1}$) and effective mass (m_{eff}) are shown in Fig. 7 for the leading backgrounds with blue, green, and magenta colored solid lines corresponding to ZZ + jets, $t\bar{t}Z$ + jets, and WWZ + jets, respectively. The signal benchmark points BP4, BP5, and BP6 are shown by yellow, cyan, and red filled regions, respectively.

Similar to HL-LHC analysis, from the Fig. 7, we can see that the distributions corresponding to the SM backgrounds peak at lower p_T values and the signal distributions are considerably more spread out peaking at much higher p_T values. Consequently, we have chosen the $p_T^{l_1} > 150$ cut at the generation level to generate the SM background processes in order to save computation time. The cross sections and the yields after the p_T cut of all the SM

TABLE VI. Comparison of signal significance of benchmark points BP1, BP2, and BP3 for different model scenarios (defined in Table II) with 0% (5%) systematic uncertainty are shown here. The numbers in last row represents the projected 95% C.L. 2σ exclusion limits on NLSP masses for a fixed 800 GeV LSP with 0% (20%) systematic uncertainty. Here, all the masses are in GeV.

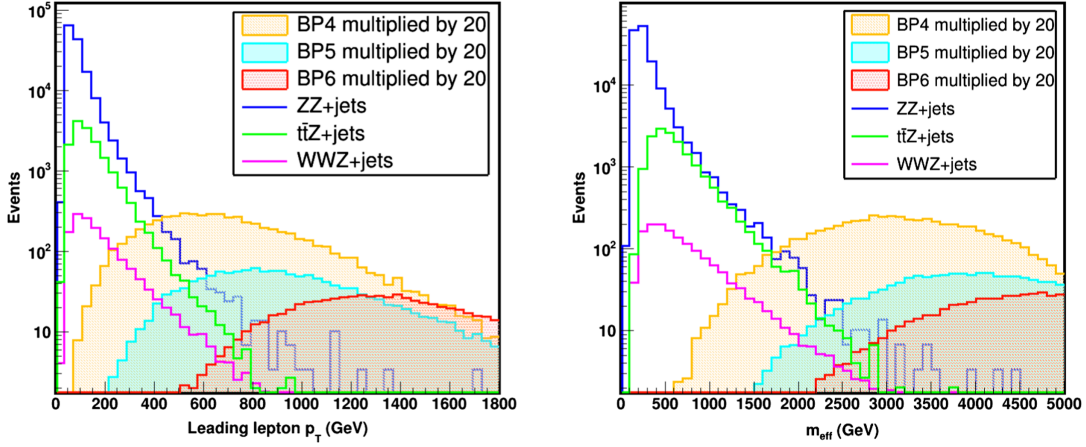| Benchmark points	Signal significance (sys. unc = 5%)			
	Scenario-I	Scenario-II	Scenario-III	Scenario-IV
BP1	12.61 (10.54)	9.49 (8.49)	5.95 (5.67)	4.21 (4.1)
BP2	8.48 (7.78)	6.45 (6.11)	4.14 (4.03)	2.96 (2.92)
BP3	5.57 (5.35)	4.21 (4.11)	2.85 (2.82)	1.51 (1.5)
$m_{\tilde{\chi}_1^0}$	Projected exclusion on $m_{\tilde{\chi}_1^\pm}$ at the HL-LHC (sys. unc. = 20%)			
800	2340 (2275)	2240 (2175)	2050 (1985)	1935 (1870)

FIG. 7. Distributions of transverse momentum of leading lepton $p_T^{l_1}$ (left panel) and effective mass m_{eff} (right panel) at the HE-LHC. The blue, green, and magenta color solid lines represent the most dominant $ZZ + \mathrm{jets}$, $t\bar{t}Z + \mathrm{jets}$ and $WWZ + \mathrm{jets}$ backgrounds respectively. Yellow, cyan, and red filled regions correspond to the benchmark points—BP4, BP5, and BP6 respectively.

background processes are summarized in Table XIII of Appendix-C. From the distribution of m_{eff} variable shown in Fig. 7, it is evident that the distributions for the SM processes peak at a much lower value of m_{eff} compared to those of the signal benchmark points. By optimizing the signal regions for different kinematic variables, we have found that similar to the 14 TeV analysis, a combination of m_{eff} variable with Z veto and b-jet veto maximize the signal

significance for the $N_l \geq 4$ final state. The cut-flow table for the signal benchmark points and the SM background channels are summarized in the Table VII. The signal significances for the benchmark points with and without a 5% uncertainty are also shown in the Table VII for our two signal regions. We have obtained $\sigma_{ss} = 12.35\,(11.90)$, 5.61 (6.35), and $3.58\,(4.47)$ for BP4, BP5, and BP6, respectively for SR-C (SR-D). It is evident that SR-D signal region is

TABLE VII. Selection cuts and the corresponding yields for three signal benchmark points and background channels at HE-LHC with $\mathcal{L} = 3000\ \mathrm{fb}^{-1}$ are shown here. Statistical signal significance (σ_{ss}) without any systematic uncertainty for BP4, BP5, and BP6 are also shown. Corresponding signal significance σ_{ss}^{ϵ} with sys. unc. $\epsilon = 5\%$ are presented in parenthesis. Here, the SUSY signals belong to scenario-I.

| Cut variables	$N_l \geq 4$ $(l = e, \mu) + p_T^{l_1} > 150$ GeV	Z veto	b veto	Signal region SR-C ($m_{\mathrm{eff}} > 1500$)	SR-D ($m_{\mathrm{eff}} > 2200$)
BP4	307.61	266.84	179.46	173.43	147.48
BP5	71.72	69.89	47.51	47.31	45.54
BP6	41.19	39.57	25.06	24.97	24.77
$ZZ + \mathrm{jets}$	15980	125.38	108.31	6.01	1.2
$t\bar{t}Z + \mathrm{jets}$	5814	467.27	103.94	6.77	1.73
$WWZ + \mathrm{jets}$	742.03	57.42	47.49	8.21	2.30
$WZZ + \mathrm{jets}$	414.87	7.93	6.02	1.09	0.27
$ZZZ + \mathrm{jets}$	142.17	1.47	1.06	0.08	0.02
h via GGF	3490	34.51	29.30	1.47	0.33
hjj	40.59	9.92	7.86	0.07	0
$Wh + \mathrm{jets}$	9.81	3.04	2.53	0.04	0.003
$Zh + \mathrm{jets}$	7.08	1.42	1.06	0.02	0.003
Total background				23.76	5.86
Signal significance σ_{ss} (σ_{ss}^{ϵ}, sys. unc. $= 5\%$)			BP4	12.35 (10.10)	11.90 (10.12)
			BP5	5.61 (5.17)	6.35 (5.98)
			BP6	3.58 (3.37)	4.47 (4.31)
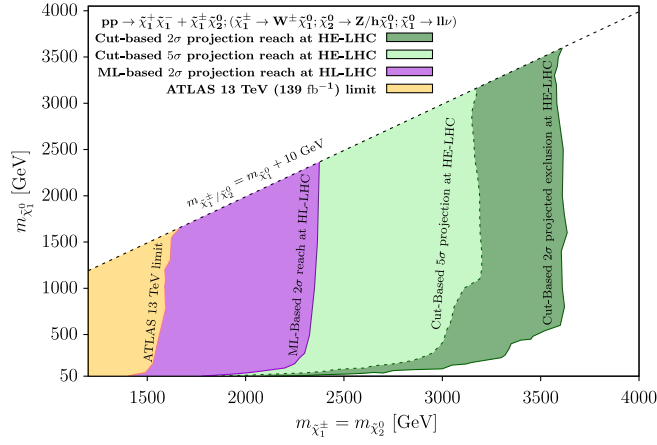
FIG. 8. Projected discovery (5σ) and exclusion (2σ) regions in the $m_{\tilde{\chi}_2^0} - m_{\tilde{\chi}_1^0}$ mass plane at the HE-LHC via conventional cut-and-count method are presented with light and dark green colors. Also, the dark violet color region corresponds to 2σ reach at HL-LHC obtained by ML-based analysis, which is already summarized in Sec III B. The yellow regions represents the existing limit obtained by the ATLAS Collaboration from run-II data [112].

more effective for the higher $m_{\tilde{\chi}_1^\pm}$ mass. The signal to background yield ratio (S/B) at 27 TeV of BP4, BP5, and BP6 are $\sim$25, (14), 8 (2), 4 (1), respectively, for SR-D (SR-C). Because of the large S/B ratio for SR-D, the changes in σ_{ss} is less significant when systematic uncertainty is considered to be nonzero. For SR-D, the signal significance (σ_{ss}) reduces by 3%–15% in the presence of 5% systematic uncertainty.

For HE-LHC, we now show the projected discovery region (with $\sigma_{ss} \geq 5$) and exclusion region (with $\sigma_{ss} \geq 2$) in Fig. 8 with light and dark green colors, respectively, for scenario-I. The dark violet color region corresponds to 2σ projection at HL-LHC obtained by ML-based analysis

which is already displayed in Fig. 6 in Sec. III B, and the yellow region is the current limits obtained by the ATLAS Collaboration using run-II data [112]. We find that 95% C.L. projected exclusion limits on $m_{\tilde{\chi}_2^0} = m_{\tilde{\chi}_1^\pm}$ reaches up to $\sim$3.5 (3.6) TeV at the HE-LHC for $\tilde{\chi}_1^0 > 500$ (1000) GeV. We also obtain that the 5σ projected discovery reach will be around 3.16 TeV. Now we proceed to compare our results corresponding to SR-D for the four different scenarios (scenario-I, II, III, IV) defined in Table II in Sec. II. The results are summarized in Table VIII. As in the 14 TeV case, the signal significance steadily decreases with increasing τ lepton multiplicity in the final state with scenario IV being the least sensitive of all. σ_{ss} are quoted for the three benchmark points with systematic uncertainty 0% (5%). The last row represents the projected 2σ exclusion limit on the wino masses at 95% C.L. keeping the LSP mass fixed at 1200 GeV with 0% (20%) systematic uncertainty. We find that the projected 2σ limit will be $\sim$800 GeV weaker for scenario-IV compare to the other extreme model i.e., scenario-I.

D. Prospect at the HE-LHC using machine learning based analysis

We have used a similar ML algorithm as discussed in Sec. III B to improve the cut-based analysis results for HE-LHC. For the ML analysis, we have considered the same set of 18 features and followed the same procedure for training, testing, hyper-parameter selection etc. as described in Sec. III B. The Shapley feature importance plot for the top ten kinematic variables and the variation of signal significance as a function of probability score for HE-LHC are presented in Fig. 9. We observe an almost similar SHAP ranking in features compared to HL-LHC analysis, and the most important features are N_Z, m_{eff}, $p_T^{l_2}$, and $p_T^{l_1}$ for HE-LHC analysis.

TABLE VIII. Comparison of signal significance of benchmark points BP4, BP5, and BP6 for different model scenarios (defined in Table II) with 0% (5%) systematic uncertainty are shown here. The numbers in last row represents the projected 95% C.L. 2σ exclusion limits on NLSP masses for a fixed 1200 GeV LSP with 0% (20%) systematic uncertainty. Here, all the masses are in GeV.

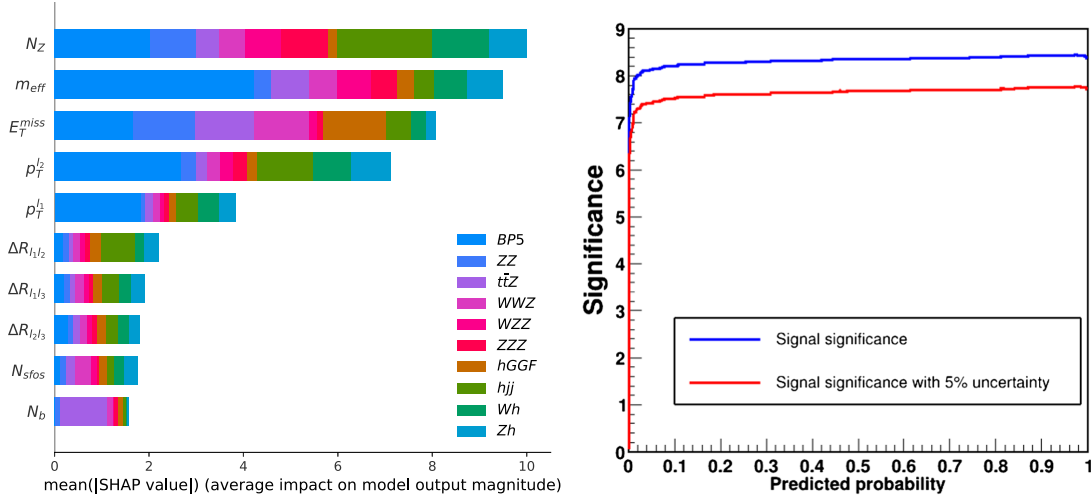| Benchmark points	Cut based signal significance (sys. unc = 5%)			
	Scenario-I	Scenario-II	Scenario-III	Scenario-IV
BP4	11.90 (10.12)	8.67 (7.86)	5.96 (5.64)	3.02 (2.96)
BP5	6.35 (5.98)	4.67 (4.49)	2.77 (2.71)	1.66 (1.64)
BP6	4.47 (4.31)	3.23 (3.15)	1.83 (1.80)	1.06 (1.05)
$m_{\tilde{\chi}_1^0}$	Projected exclusion on $m_{\tilde{\chi}_1^\pm}$ at the HE-LHC (sys. unc = 20%)			
1200	3620 (3480)	3400 (3260)	3080 (2940)	2780 (2640)

FIG. 9. (Left) Shapley feature importance plot for the top ten kinematic variables for the dataset with benchmark SUSY signal BP5 ($m_{\tilde{\chi}_1^\pm} = 2900$, $m_{\tilde{\chi}_1^0} = 1200$) and backgrounds analyzed at HE-LHC. (Right) The signal significance for BP5 without any systematic uncertainty (blue line) and with 5% systematic uncertainty (red line) as a function of predicted probability are shown.

In Table IX, the signal yield, total backgrounds yield, signal significance with 0% and 5% systematic uncertainty for the representative benchmark points BP4, BP5, and BP6 are displayed for probability score 0.90 and 0.96. We notice that there are around ~30%–50% gains in signal significance compared to the cut-and-count method. The gain is also reflected in the projected exclusion plot (Fig. 10) displayed in the LSP-NLSP mass plane. We find that the projected discovery limit reaches up to 3.3 TeV (illustrated in light red color) in ML-based analysis, which is around 140 GeV larger than the cut-based reach. Also, the projected exclusion limit extends up to ~4.0 TeV (presented by dark red color in Fig. 10) resulting a 380 GeV enhancement from the traditional cut-and-count method. The dark violet and dark green region correspond

to ML-based 2σ reach at the HL-LHC and cut-based 2σ reach at the HE-LHC, respectively, which is summarized in Sec. III B and Sec. III C.

Now we proceed to study the effect of choosing different couplings or SUSY scenarios as defined in Table II. The signal significance for BP4, BP5, and BP6 and the projected 2σ exclusion limits on $m_{\tilde{\chi}_1^\pm}$ for fixed $m_{\tilde{\chi}_1^0} = 1200$ GeV are listed in Table VIII. As expected the maximum reach is obtained for scenario-I (3.94 TeV) and scenario-IV corresponds to the least sensitive compare to others (3.2 TeV). The effect of systematic uncertainty are also displayed in Table X. It may be noted that the projected exclusion limits on $m_{\tilde{\chi}_1^\pm}$ as mentioned in Table X improve by ~50–60 GeV if the LSP-NLSP mass gap is ~10 GeV.

TABLE IX. Signal yield, total background yield, and the signal significance (without any systematic uncertainty) at the HE-LHC using ML-based algorithm for different probability scores are presented here. The numbers in the parenthesis correspond to σ_{ss} with systematic uncertainty $\epsilon = 5\%$. Here, the SUSY signal belongs to scenario-I.

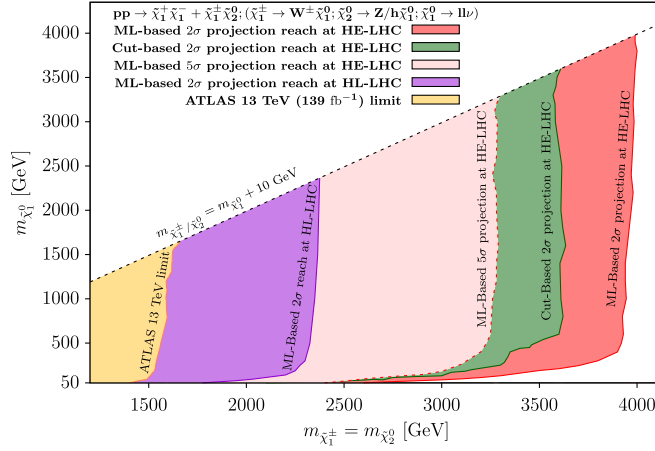| Benchmark points	Probability score	Signal yield	Total background yield	Signal significance σ_{ss} (sys. unc = 5%)	Gain in σ_{ss} from cut based
BP4	0.90	356.72	7.46	18.69 (13.52)	51% (34%)
	0.96	352.86	6.25	18.62 (13.51)	51% (34%)
BP5	0.90	71.80	0.94	8.42 (7.74)	33% (29%)
	0.96	71.54	0.78	8.41 (7.74)	32% (29%)
BP6	0.90	41.27	0.83	6.36 (6.05)	42% (40%)
	0.96	41.20	0.08	6.41 (6.10)	43% (41%)

FIG. 10. Projected discovery (5σ) and exclusion (2σ) regions in the $m_{\tilde{\chi}_2^0} - m_{\tilde{\chi}_1^0}$ mass plane at the HE-LHC are presented with light and dark red colors. The green and dark violet color region represent the 2σ reach obtained by cut-based analysis at the HE-LHC and ML-based analysis at the HL-LHC, respectively. The yellow regions represents the existing limit obtained by the ATLAS Collaboration from run-II data [112].

TABLE X. Comparison of signal significance of benchmark points BP4, BP5, and BP6 for different model scenarios (defined in Table II) with 0% (5%) systematic uncertainty are shown here. The numbers in last row represents the projected 95% C.L. 2σ exclusion limits on NLSP masses for a fixed 1200 GeV LSP with 0% (20%) systematic uncertainty. Here, all the masses are in GeV.

Benchmark points	*ML* based signal significance (sys. unc = 5%)			
	Scenario-I	Scenario-II	Scenario-III	Scenario-IV
BP4	18.69 (13.52)	12.72 (10.63)	7.99 (7.36)	5.21 (4.99)
BP5	8.42 (7.74)	6.4 (6.09)	4.21 (4.11)	2.97 (2.93)
BP6	6.36 (6.05)	4.98 (4.83)	3.23 (3.19)	2.31 (2.29)
$m_{\tilde{\chi}_1^0}$	Projected exclusion on $m_{\tilde{\chi}_1^\pm}$ at the HE-LHC (sys. unc = 20%)			
1200	3940 (3850)	3790 (3700)	3450 (3360)	3200 (3115)

IV. CONCLUSION

Supersymmetry remains one of the most highly motivated beyond the SM scenario both theoretically and phenomenologically. In the absence of any significant excess over the SM from the experimental results, it is important to study the existing models under existing data and assess how much of the relevant parameter space can be probed at the highest luminosity of the LHC. In the process, the canonical search techniques are to be put to comparison with the new tools available at our disposal at present to assess how much we can improve on the existing sensitivities. The gaugino sector of the supersymmetry has diverse phenomenological implications and hence, is of

very high interest. The gaugino sector of the R-parity conserving MSSM has been studied exhaustively in this regard while the various R-parity violating scenarios have not been explored to that extent. In this work, we have chosen a multilepton ($N_l \geq 4$ with $l \equiv e$, μ) final state to assess the discovery and exclusion reach of the high luminosity LHC as well as the high energy LHC in terms of the gaugino masses. We have compared the sensitivity of probing the parameter space through traditional cut-based method and machine learning based method. Our results clearly show that one can expect a gain of up to 43% and 51% in signal significance using the gradient boosted decision tree algorithm over that of the cut based analyses in the context of the HL-LHC and HE-LHC, respectively. This leads to a far better reach in the exclusion and discovery limits in the wino-bino mass plane. For scenarios with nonzero λ_{121} and/or λ_{122}, the projected discovery reach at the HL-LHC, obtained by us are $\sim$1.99 TeV and $\sim$1.87 TeV in ML-based and cut-based methods, respectively. Similarly, the projected exclusion curve reaches upto $\sim$2.37 TeV and $\sim$2.18 TeV, respectively. At the HE-LHC, ML-based method provides even better sensitivity. Our projected 5σ discovery sensitivity reaches up to $\sim$3.3 TeV in ML-based analysis which is $\sim$140 GeV larger than that of the cut-based reach. The projected exclusion limit reaches $\sim$4 TeV which is an improvement by $\sim$380 GeV over the corresponding cut-based analysis. Apart from the scenarios with nonzero λ_{121} and/or λ_{122}, we also discuss the possibility of three other scenarios, derived from the remaining seven nonzero single λ_{ijk} couplings, with varied τ lepton multiplicity in the final state. With specific choices of benchmark points, we show how the sensitivities vary for these different scenarios for $N_l \geq 4$ final state.

APPENDIX A: BACKGROUND CROSS SECTIONS AT THE HL-LHC

To make sure that the yields from the tails saturate, for different background event distributions, we have simulated a larger number of raw events compared to what would be expected from weighing according to the cross sections, luminosity, and leptonic branching ratios. In order to save the computation time and ensure that we have sufficient events in the high kinematic region, we generate the events with W/Z bosons decaying explicitly into leptonic final state along with a cut on the leading lepton momentum, $p_T^{l_1} > 100$ GeV at the parton level generation (done using MadGraph) itself. As mentioned in the last column of Table 11 in Appendix A, we have enlisted the weighted numbers of background events (N) at the

TABLE XI. Cross sections for various relevant SM backgrounds at the 14 TeV LHC are shown here. The corresponding number for $4l$ final states by multiplying the appropriate branching ratios and the yields at the HL-LHC after applying a generation level cut $p_T^{l_1} > 100$ GeV are presented in the last two column, respectively.

Background	Cross section order	Cross section σ (fb)	$\sigma' = \sigma \times$ Br. $(4l)$ (fb)	Yield at the HL-LHC after generation level cut $p_T^{l_1} > 100$ GeV
$ZZ +$ jets	NNLO [135]	18.77×10^3	86.79	53640
$t\bar{t}Z +$ jets	NLO [136]	1.018×10^3	3.35	5931
$WWZ +$ jets	NLO [137]	181.7	0.598	1059
$WZZ +$ jets	NLO [122]	64	0.296	516
$ZZZ +$ jets	NLO [137]	15.3	0.197	282
h (via GGF)	N3LO QCD + NLO EW [138]	54.72×10^3	7.037	3042
hjj	NLO [122]	6.42×10^3	0.826	381
$Wh +$ jets	NNLO QCD + NLO EW [138]	1.498×10^3	0.193	78
$Zh +$ jets	NNLO QCD + NLO EW [138]	981	0.126	50.1

HL-LHC, where N = cross section $(\sigma) \times \mathcal{L} \times$ Br$(4l) \times \epsilon$. Here, $\mathcal{L}$ is the integrated luminosity = 3000 fb^{-1} and ϵ is the efficiency of $p_T^{l_1} > 100$ GeV cut ($l = e$, μ, and l_1 is leading lepton). But to produce a saturated tail and reliable results, we have generated $\sim 8 \times 10^5$ ZZ & $\sim 3 \times 10^5$ $t\bar{t}Z$ events. For the other remaining backgrounds, we have generated $\sim 1 \times 10^5$ events each. A similar approach has been followed for HE-LHC background generation.

APPENDIX B: SIGNAL CROSS SECTIONS AT THE HL-LHC AND HE-LHC

TABLE XII. NLO + NLL cross sections for the 14 TeV and 27 TeV LHC for signal benchmark points obtained using [124].

Signal $(m_{\tilde{\chi}_1^\pm/\tilde{\chi}_2^0}, m_{\tilde{\chi}_1^0})$ GeV	Cross section σ (fb) at 14 TeV (NLO + NLL)	Signal $(m_{\tilde{\chi}_1^\pm/\tilde{\chi}_2^0}, m_{\tilde{\chi}_1^0})$ GeV	Cross section σ (fb) at 27 TeV (NLO + NLL)
BP1 (1600,250)	0.107	BP4 (2300,250)	0.219
BP2 (1800,800)	0.042	BP5 (2900,1200)	0.042
BP2 (1950,1850)	0.019	BP6 (3100,3000)	0.025

APPENDIX C: BACKGROUND CROSS SECTIONS AT THE HE-LHC

TABLE XIII.   Cross sections at the 27 TeV LHC for various SM backgrounds considered in this analysis are shown here. Conventions are same as in Table XI. The last column represents the yields at the HE-LHC after applying a generation level cut $p_T^{l_1} > 150$ GeV.

Background	Cross section order	Cross section σ (fb)	$\sigma' = \sigma \times$ Br. $(4l)$ (fb)	Yield at the HE-LHC after generation level cut $p_T^{l_1} > 150$ GeV
ZZ + jets	NNLO [136]	44.52×10^3	205.86	53730
$t\bar{t}Z$ + jets	NLO [136]	4.9×10^3	16.126	16740
WWZ + jets	NLO [122]	573.04	1.886	2355
WZZ + jets	NLO [122]	197.1	0.911	1116
ZZZ + jets	NLO [122]	41.77	0.537	429
h (via GGF)	N3LO QCD + NLO EW [138]	146.65×10^3	18.859	6675
hjj	NLO [122]	15.977×10^3	2.05	308
Wh + jets	NNLO QCD + NLO EW [138]	3.397×10^3	0.437	63
Zh + jets	NNLO QCD + NLO EW [138]	2.463×10^3	0.317	45

APPENDIX D: VALIDATION OF ATLAS RESULT

We compare the experimental results with those of our simulation to validate our analysis. In order to do so, we look at signal regions $SR0_{\text{bveto}}^{\text{loose}}$ and $SR0_{\text{bveto}}^{\text{tight}}$ considered by the ATLAS Collaboration [112] and reproduce the cut-flow table. As shown below in Table XIV, the numbers agree reasonable deviation at most by 10%. The experimental collaboration also provides a 95% C.L. exclusion contour in the bino-wino mass plane, which we reproduced through our analysis. A comparison between the two results is shown in Fig. 11. The dotted magenta line and the solid blue line represent the experimental result and our simulation result, respectively. As evident, we have a nice agreement, especially for lower bino LSP masses.

TABLE XIV.   Cut flow table for the signal regions $SR0_{\text{bveto}}^{\text{loose}}$ and $SR0_{\text{bveto}}^{\text{tight}}$ considered by the ATLAS Collaboration in Ref. [112]. The second column represents the event yields provided by the ATLAS Collaboration in Ref. [139] (Auxiliary material for Ref. [112]). The yields originating from our simulation setup are presented in the third column. Here, wino production ($\tilde{\chi}_1^\pm \tilde{\chi}_1^\mp$, $\tilde{\chi}_1^\pm \tilde{\chi}_2^0$) events are considered for $m_{\tilde{\chi}_1^\pm} = 1300$ GeV, $m_{\tilde{\chi}_1^0} = 800$ GeV) at $\sqrt{s} = 13$ TeV with $\mathcal{L} = 139$ fb^{-1}.

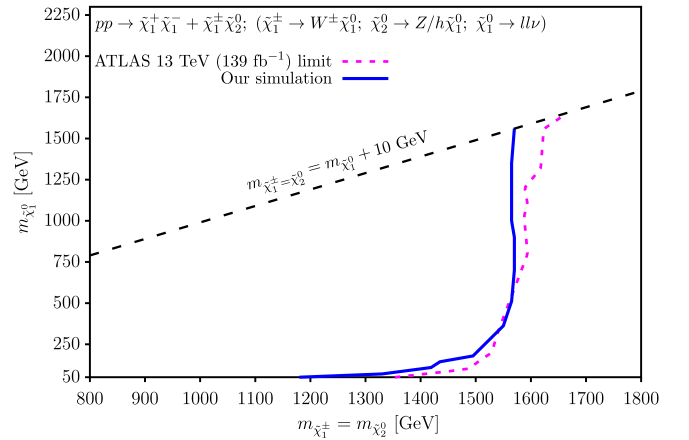|	Yield ($\sigma \times \mathcal{L} \times \epsilon$)	
Cuts	ATLAS result	Our simulation
Total production (without any cut)	49.54	49.48
$N_l \geq 4$	32.65	29.35
Z veto	30.75	27.57
b veto	16.08	16.76
$m_{\text{eff}} > 600$ GeV ($SR0_{\text{bveto}}^{\text{loose}}$)	16.07	16.75
$m_{\text{eff}} > 1250$ GeV ($SR0_{\text{bveto}}^{\text{tight}}$)	15.50	15.58

FIG. 11.   Comparison of the 95% C.L. exclusion limit obtained by ATLAS run-II data [112] and our analysis. The magenta colored dotted line represents the limit obtained by ATLAS, and the blue solid line corresponds to the exclusion reach obtained from our analysis.

[1] S. P. Martin, A supersymmetry primer, Adv. Ser. Dir. High Energy Phys. **18**, 1 (1998).

[2] M. Drees, P. Roy, and R. Godbole, *Theory and Phenomenology of Sparticles: An Account of Four-Dimensional N* (World Scientific, Singapore, 2004), 10.1142/4001.

[3] H. Baer and X. Tata, *Weak Scale Supersymmetry: From Superfields to Scattering Events* (Cambridge University Press, Cambridge, England, 2006).

[4] L. Susskind, The gauge hierarchy problem, technicolor, supersymmetry, and all that, Phys. Rep. **104**, 181 (1984).

[5] E. Gildener, Gauge-symmetry hierarchies, Phys. Rev. D **14**, 1667 (1976).

[6] F. Zwicky, Die Rotverschiebung von extragalaktischen Nebeln, Helv. Phys. Acta **6**, 110 (1933).

[7] F. Zwicky, On the masses of nebulae and of clusters of nebulae, Astrophys. J. **86**, 217 (1937).

[8] Y. Sofue and V. Rubin, Rotation curves of spiral galaxies, Annu. Rev. Astron. Astrophys. **39**, 137 (2001).

[9] G. Jungman, M. Kamionkowski, and K. Griest, Supersymmetric dark matter, Phys. Rep. **267**, 195 (1996).

[10] A. Gando *et al.* (KamLAND Collaboration), Reactor on-off antineutrino measurement with KamLAND, Phys. Rev. D **88**, 033001 (2013).

[11] G. Bellini *et al.* (Borexino Collaboration), Final results of Borexino Phase-I on low energy solar neutrino spectroscopy, Phys. Rev. D **89**, 112007 (2014).

[12] G. Bak *et al.* (RENO Collaboration), Measurement of reactor antineutrino oscillation amplitude and frequency at RENO, Phys. Rev. Lett. **121**, 201801 (2018).

[13] K. Abe *et al.* (T2K Collaboration), Search for *CP* violation in neutrino and antineutrino oscillations by the T2K experiment with 2.2×10^{21} protons on target, Phys. Rev. Lett. **121**, 171802 (2018).

[14] D. Adey *et al.* (Daya Bay Collaboration), Measurement of the electron antineutrino oscillation with 1958 days of operation at Daya Bay, Phys. Rev. Lett. **121**, 241805 (2018).

[15] M. Jiang *et al.* (Super-Kamiokande Collaboration), Atmospheric neutrino oscillation analysis with improved event reconstruction in Super-Kamiokande IV, Prog. Theor. Exp. Phys. **2019**, 053F01 (2019).

[16] M. A. Acero *et al.* (NOvA Collaboration), First measurement of neutrino oscillation parameters using neutrinos and antineutrinos by NOvA, Phys. Rev. Lett. **123**, 151803 (2019).

[17] R. Aaij *et al.* (LHCb Collaboration), Direct *CP* violation in charmless three-body decays of B± mesons, Phys. Rev. D **108**, 012008 (2023).

[18] J. P. Lees *et al.* (*BABAR* Collaboration), Search for mixing-induced *CP* violation using partial reconstruction of $\bar{B}^0 \to D^{*+}X\ell^-\bar{\nu}_\ell$ and kaon tagging, Phys. Rev. D **93**, 032001 (2016).

[19] L. K. Li *et al.* (Belle Collaboration), Search for *CP* violation and measurement of branching fractions and decay asymmetry parameters for $\Lambda_c^+ \to \Lambda_h^+$ and $\Lambda_c^+ \to \Sigma^0 h^+ (h = K, \pi)$, Sci. Bull. **68**, 583 (2023).

[20] T. A. Aaltonen *et al.* (CDF Collaboration), Measurements of direct *CP*-violating asymmetries in charmless decays of bottom baryons, Phys. Rev. Lett. **113**, 242001 (2014).

[21] H. Miao (BESIII Collaboration), Measurements of charmonia decays from BESIII, in *Proceedings of the 21st Conference on Flavor Physics and CP Violation* (2023), arXiv:2307.12565.

[22] J. Ellis, S. Kelley, and D. Nanopoulos, Precision lep data, supersymmetric guts and string unification, Phys. Lett. B **249**, 441 (1990).

[23] U. Amaldi, W. de Boer, and H. Fürstenau, Comparison of grand unified theories with electroweak and strong coupling constants measured at LEP, Phys. Lett. B **260**, 447 (1991).

[24] G. Ross and R. Roberts, Minimal supersymmetric unification predictions, Nucl. Phys. **B377**, 571 (1992).

[25] CMS SUSY public result, https://cms-results.web.cern.ch/cms-results/public-results/preliminary-results/SUS/index.html.

[26] ATLAS SUSY public result, https://twiki.cern.ch/twiki/bin/view/AtlasPublic/SupersymmetryPublicResults.

[27] G. Aad *et al.* (ATLAS Collaboration), Search for squarks and gluinos in final states with jets and missing transverse momentum using 139 fb⁻¹ of $\sqrt{s} = 13$ TeV pp collision data with the ATLAS detector, J. High Energy Phys. 02 (2021) 143.

[28] A. M. Sirunyan *et al.* (CMS Collaboration), Search for top squark production in fully-hadronic final states in proton-proton collisions at $\sqrt{s} = 13$ TeV, Phys. Rev. D **104**, 052001 (2021).

[29] G. Aad *et al.* (ATLAS Collaboration), Search for squarks and gluinos in final states with one isolated lepton, jets, and missing transverse momentum at $\sqrt{s} = 13$ with the ATLAS detector, Eur. Phys. J. C **81**, 600 (2021).

[30] A. Tumasyan *et al.* (CMS Collaboration), Search for supersymmetry in final states with two or three soft leptons and missing transverse momentum in proton-proton collisions at $\sqrt{s} = 13$ TeV, J. High Energy Phys. 04 (2022) 091.

[31] G. Aad *et al.* (ATLAS Collaboration), Search for charginos and neutralinos in final states with two boosted hadronically decaying bosons and missing transverse momentum in pp collisions at $\sqrt{s} = 13$ TeV with the ATLAS detector, Phys. Rev. D **104**, 112010 (2021).

[32] G. Aad *et al.* (ATLAS Collaboration), Search for direct production of winos and Higgsinos in events with two same-charge leptons or three leptons in pp collision data at $\sqrt{s} = 13$ TeV with the ATLAS detector, J. High Energy Phys. 11 (2023) 150.

[33] G. Aad *et al.* (ATLAS Collaboration), Search for direct pair production of sleptons and charginos decaying to two leptons and neutralinos with mass splittings near the W-boson mass in $\sqrt{s} = 13$ TeV pp collisions with the ATLAS detector, J. High Energy Phys. 06 (2023) 031.

[34] G. Aad *et al.* (ATLAS Collaboration), Search for chargino–neutralino pair production in final states with three leptons and missing transverse momentum in $\sqrt{s} = 13$ TeV pp collisions with the ATLAS detector, Eur. Phys. J. C **81**, 1118 (2021).

[35] A. M. Sirunyan *et al.* (CMS Collaboration), Search for supersymmetry in final states with two oppositely charged same-flavor leptons and missing transverse momentum in

proton-proton collisions at $\sqrt{s} = 13$ TeV, J. High Energy Phys. 04 (2021) 123.

[36] A. M. Sirunyan *et al.* (CMS Collaboration), Search for supersymmetry with a compressed mass spectrum in the vector boson fusion topology with 1-lepton and 0-lepton final states in proton-proton collisions at $\sqrt{s} = 13$ TeV, J. High Energy Phys. 08 (2019) 150.

[37] A. Tumasyan *et al.* (CMS Collaboration), Search for electroweak production of charginos and neutralinos in proton-proton collisions at $\sqrt{s} = 13$ TeV, J. High Energy Phys. 04 (2022) 147.

[38] CMS Collaboration, Search for electroweak production of supersymmetric particles in final states containing hadronic decays of WW, WZ, or WH and missing transverse momentum, Phys. Lett. B **842**, 137460 (2023).

[39] H. K. Dreiner, An introduction to explicit R-parity violation, Adv. Ser. Dir. High Energy Phys. **21**, 565 (2010).

[40] R. Barbier *et al.*, R-parity violating supersymmetry, Phys. Rep. **420**, 1 (2005).

[41] T. Banks, Y. Grossman, E. Nardi, and Y. Nir, Supersymmetry without R-parity and without lepton number, Phys. Rev. D **52**, 5319 (1995).

[42] H. K. Dreiner, Y. S. Koay, D. Köhler, V. M. Lozano, J. Montejo Berlingen, S. Nangia, and N. Strobbe, The ABC of RPV: Classification of R-parity violating signatures at the LHC for small couplings, J. High Energy Phys. 07 (2023) 215.

[43] R. K. Barman, B. Bhattacherjee, I. Chakraborty, A. Choudhury, and N. Khan, Electroweakino searches at the HL-LHC in the baryon number violating MSSM, Phys. Rev. D **103**, 015003 (2021).

[44] V. A. Mitsou, R-parity violating supersymmetry and neutrino physics: Experimental signatures, Proc. Sci. PLANCK2015 (**2015**) 085.

[45] D. Bardhan, A. Chakraborty, D. Choudhury, D. K. Ghosh, and M. Maity, Search for bottom squarks in the baryon-number violating MSSM, Phys. Rev. D **96**, 035024 (2017).

[46] B. Bhattacherjee and A. Chakraborty, Study of the baryonic R-parity violating MSSM using the jet substructure technique at the 14 TeV LHC, Phys. Rev. D **89**, 115016 (2014).

[47] B. Bhattacherjee, J. L. Evans, M. Ibe, S. Matsumoto, and T. T. Yanagida, Natural supersymmetry's last hope: R-parity violation via UDD operators, Phys. Rev. D **87**, 115002 (2013).

[48] D. Dercks, J. De Vries, H. K. Dreiner, and Z. S. Wang, R-parity violation and light neutralinos at CODEX-b, FASER, and MATHUSLA, Phys. Rev. D **99**, 055039 (2019).

[49] A. Choudhury, A. Mondal, S. Mondal, and S. Sarkar, Slepton searches in the trilinear RPV SUSY scenarios at the HL-LHC and HE-LHC, arXiv:2310.07532.

[50] G. Aad *et al.* (ATLAS Collaboration), Search for R-parity-violating supersymmetry in a final state containing leptons and many jets with the ATLAS experiment using $\sqrt{s} = 13$ TeV proton–proton collision data, Eur. Phys. J. C **81**, 1023 (2021).

[51] G. Aad *et al.* (ATLAS Collaboration), Search for phenomena beyond the Standard Model in events with large b-jet

multiplicity using the ATLAS detector at the LHC, Eur. Phys. J. C **81**, 11 (2021).

[52] G. Aad *et al.* (ATLAS Collaboration), Search for squarks and gluinos in final states with same-sign leptons and jets using 139 fb^{-1} of data collected with the ATLAS detector, J. High Energy Phys. 06 (2020) 046.

[53] M. Aaboud *et al.* (ATLAS Collaboration), Search for R-parity-violating supersymmetric particles in multi-jet final states produced in p-p collisions at $\sqrt{s} = 13$ TeV using the ATLAS detector at the LHC, Phys. Lett. B **785**, 136 (2018).

[54] A. M. Sirunyan *et al.* (CMS Collaboration), Search for top squarks in final states with two top quarks and several light-flavor jets in proton-proton collisions at $\sqrt{s} = 13$ TeV, Phys. Rev. D **104**, 032006 (2021).

[55] A. M. Sirunyan *et al.* (CMS Collaboration), Search for resonant production of second-generation sleptons with same-sign dimuon events in proton-proton collisions at $\sqrt{s} = 13$ TeV, Eur. Phys. J. C **79**, 305 (2019).

[56] A. M. Sirunyan *et al.* (CMS Collaboration), Search for R-parity violating supersymmetry in pp collisions at $\sqrt{s} = 13$ TeV using b jets in a final state with a single lepton, many jets, and high sum of large-radius jet masses, Phys. Lett. B **783**, 114 (2018).

[57] V. Khachatryan *et al.* (CMS Collaboration), Search for R-parity violating supersymmetry with displaced vertices in proton-proton collisions at $\sqrt{s} = 8$ TeV, Phys. Rev. D **95**, 012009 (2017).

[58] V. Khachatryan *et al.* (CMS Collaboration), Searches for R-parity-violating supersymmetry in pp collisions at $\sqrt{s} = 8$ TeV in final states with 0-4 leptons, Phys. Rev. D **94**, 112009 (2016).

[59] S. Chatrchyan *et al.* (CMS Collaboration), Search for top squarks in R-parity-violating supersymmetry using three or more leptons and B-tagged jets, Phys. Rev. Lett. **111**, 221801 (2013).

[60] G. Aad *et al.* (ATLAS Collaboration), Summary of the searches for squarks and gluinos using $\sqrt{s} = 8$ TeV pp collisions with the ATLAS experiment at the LHC, J. High Energy Phys. 10 (2015) 054.

[61] G. Aad *et al.* (ATLAS Collaboration), Search for squarks and gluinos in events with isolated leptons, jets and missing transverse momentum at $\sqrt{s} = 8$ TeV with the ATLAS detector, J. High Energy Phys. 04 (2015) 116.

[62] F. M. Borzumati, Y. Grossman, E. Nardi, and Y. Nir, Neutrino masses and mixing in supersymmetric models without R parity, Phys. Lett. B **384**, 123 (1996).

[63] Y. Grossman and S. Rakshit, Neutrino masses in R-parity violating supersymmetric models, Phys. Rev. D **69**, 093002 (2004).

[64] A. Choudhury, S. Mitra, A. Mondal, and S. Mondal, Bilinear R-parity violating supersymmetry under the light of neutrino oscillation, Higgs and flavor data, arXiv:2305.15211.

[65] S. Davidson and M. Losada, Neutrino masses in the R(p) violating MSSM, J. High Energy Phys. 05 (2000) 021.

[66] B. Mukhopadhyaya, S. Roy, and F. Vissani, Correlation between neutrino oscillations and collider signals of

supersymmetry in an R-parity violating model, Phys. Lett. B **443,** 191 (1998).

[67] S. Roy and B. Mukhopadhyaya, Some implications of a supersymmetric model with R-parity breaking bilinear interactions, Phys. Rev. D **55,** 7020 (1997).

[68] S. Rakshit, G. Bhattacharyya, and A. Raychaudhuri, R-parity violating trilinear couplings and recent neutrino data, Phys. Rev. D **59,** 091701 (1999).

[69] B. C. Allanach and C. H. Kom, Lepton number violating mSUGRA and neutrino masses, J. High Energy Phys. 04 (2008) 081.

[70] M. A. Díaz, M. Rivera, and N. Rojas, On neutrino masses in the MSSM with BRpV, Nucl. Phys. **B887,** 338 (2014).

[71] R. Bose, A. Datta, A. Kundu, and S. Poddar, LHC signatures of neutrino mass generation through R-parity violation, Phys. Rev. D **90,** 035007 (2014).

[72] S. P. Das, A. Datta, and S. Poddar, Top squark and neutralino decays in a R-parity violating model constrained by neutrino oscillation data, Phys. Rev. D **73,** 075014 (2006).

[73] A. Datta and S. Poddar, Probing R-parity violating models of neutrino mass at the LHC via top squark decays, Phys. Rev. D **79,** 075021 (2009).

[74] A. Chakraborty and S. Chakraborty, Probing $(g-2)_\mu$ at the LHC in the paradigm of R-parity violating MSSM, Phys. Rev. D **93,** 075035 (2016).

[75] W. Altmannshofer, P. S. B. Dev, A. Soni, and Y. Sui, Addressing $R_{D^{(*)}}$, $R_{K^{(*)}}$, muon $g-2$ and ANITA anomalies in a minimal R-parity violating supersymmetric framework, Phys. Rev. D **102,** 015031 (2020).

[76] M.-D. Zheng and H.-H. Zhang, Studying the $b \to s\ell^+\ell^-$ anomalies and $(g-2)_\mu$ in R-parity violating MSSM framework with the inverse seesaw mechanism, Phys. Rev. D **104,** 115023 (2021).

[77] M. Chakraborti, S. Iwamoto, J. S. Kim, R. Masełek, and K. Sakurai, Supersymmetric explanation of the muon g—2 anomaly with and without stable neutralino, J. High Energy Phys. 08 (2022) 124.

[78] R. Masełek, Muon g-2 in SUSY scenarios with and without stable neutralinos, in *Proceedings 56th Rencontres de Moriond on Electroweak Interactions and Unified Theories* (2022), arXiv:2205.04378.

[79] M.-D. Zheng, F.-Z. Chen, and H.-H. Zhang, Explaining anomalies of B-physics, muon $g-2$ and W mass in R-parity violating MSSM with seesaw mechanism, Eur. Phys. J. C **82,** 895 (2022).

[80] R. S. Hundi, Constraints from neutrino masses and muon (g-2) in the bilinear R-parity violating supersymmetric model, Phys. Rev. D **83,** 115019 (2011).

[81] D. Bardhan, D. Ghosh, and D. Sachdeva, RK(*) from RPV-SUSY sneutrinos, Nucl. Phys. **B986,** 116059 (2023).

[82] S. Trifinopoulos, B -physics anomalies: The bridge between R -parity violating supersymmetry and flavored dark matter, Phys. Rev. D **100,** 115022 (2019).

[83] F. Domingo, H. K. Dreiner, J. S. Kim, M. E. Krauss, M. Lozano, and Z. S. Wang, Updating bounds on R-parity violating supersymmetry from meson oscillation data, J. High Energy Phys. 02 (2019) 066.

[84] D. Das, C. Hati, G. Kumar, and N. Mahajan, Scrutinizing R-parity violating interactions in light of $R_{K^{(*)}}$ data, Phys. Rev. D **96,** 095033 (2017).

[85] R. Kumar Barman, G. Belanger, and R. M. Godbole, Status of low mass LSP in SUSY, Eur. Phys. J. Spec. Top. **229,** 3159 (2020).

[86] R. K. Barman, G. Bélanger, B. Bhattacherjee, R. M. Godbole, and R. Sengupta, Is light neutralino thermal dark matter in the phenomenological minimal supersymmetric Standard Model ruled out?, Phys. Rev. Lett. **131,** 011802 (2023).

[87] Y. He, X. Jia, L. Meng, Y. Yue, and D. Zhang, Impact of recent measurement of $(g-2)_\mu$, LHC search for supersymmetry, and LZ experiment on minimal supersymmetric Standard Model, Phys. Rev. D **108,** 115010 (2023).

[88] M. Chakraborti, U. Chattopadhyay, A. Choudhury, A. Datta, and S. Poddar, Reduced LHC constraints for higgsino-like heavier electroweakinos, J. High Energy Phys. 11 (2015) 050.

[89] M. Chakraborti, U. Chattopadhyay, A. Choudhury, A. Datta, and S. Poddar, The electroweak sector of the pMSSM in the light of LHC—8 TeV and other data, J. High Energy Phys. 07 (2014) 019.

[90] M. Chakraborti, U. Chattopadhyay, and S. Poddar, How light a Higgsino or a wino dark matter can become in a compressed scenario of MSSM, J. High Energy Phys. 09 (2017) 064.

[91] D. Chowdhury, K. M. Patel, X. Tata, and S. K. Vempati, Indirect searches of the degenerate MSSM, Phys. Rev. D **95,** 075025 (2017).

[92] N. Bhattacharyya, A. Choudhury, and A. Datta, Low mass neutralino dark matter in mSUGRA and more general models in the light of LHC data, Phys. Rev. D **84,** 095006 (2011).

[93] A. Choudhury and A. Datta, Many faces of low mass neutralino dark matter in the unconstrained MSSM, LHC data and new signals, J. High Energy Phys. 06 (2012) 006.

[94] A. Choudhury and A. Datta, Neutralino dark matter confronted by the LHC constraints on electroweak SUSY signals, J. High Energy Phys. 09 (2013) 119.

[95] H. Baer, V. Barger, and H. Serce, Anomalous muon magnetic moment, supersymmetry, naturalness, LHC search limits and the landscape, Phys. Lett. B **820,** 136480 (2021).

[96] P. Athron, C. Balazs, D. H. J. Jacob, W. Kotlarski, D. Stockinger, and H. Stockinger-Kim, New physics explanations of a_μ in light of the FNAL muon g-2 measurement, J. High Energy Phys. 09 (2021) 080.

[97] M. Endo, K. Hamaguchi, S. Iwamoto, and T. Kitahara, Supersymmetric interpretation of the muon g—2 anomaly, J. High Energy Phys. 07 (2021) 075.

[98] M. Chakraborti, L. Roszkowski, and S. Trojanowski, GUT-constrained supersymmetry and dark matter in light of the new $(g-2)_\mu$ determination, J. High Energy Phys. 05 (2021) 252.

[99] A. Choudhury, S. Rao, and L. Roszkowski, Impact of LHC data on muon $g-2$ solutions in a vectorlike extension of the constrained MSSM, Phys. Rev. D **96,** 075046 (2017).

[100] A. Choudhury, L. Darmé, L. Roszkowski, E. M. Sessolo, and S. Trojanowski, Muon $g-2$ and related phenomenology in constrained vector-like extensions of the MSSM, J. High Energy Phys. 05 (2017) 072.

[101] H. Banerjee, P. Byakti, and S. Roy, Supersymmetric gauged $U(1)_{L_\mu - L_\tau}$ model for neutrinos and the muon $(g-2)$ anomaly, Phys. Rev. D **98,** 075022 (2018).

[102] H. Banerjee, B. Dutta, and S. Roy, Supersymmetric gauged $U(1)_{L_\mu - L_\tau}$ model for electron and muon $(g-2)$ anomaly, J. High Energy Phys. 03 (2021) 211.

[103] M. Chakraborti, S. Heinemeyer, and I. Saha, The new "MUON G-2" result and supersymmetry, Eur. Phys. J. C **81,** 1114 (2021).

[104] M. Frank, Y. Hiçyılmaz, S. Mondal, O. Özdal, and C. S. Ün, Electron and muon magnetic moments and implications for dark matter and model characterisation in non-universal U(1)' supersymmetric models, J. High Energy Phys. 10 (2021) 063.

[105] M. I. Ali, M. Chakraborti, U. Chattopadhyay, and S. Mukherjee, Muon and electron $(g-2)$ anomalies with non-holomorphic interactions in MSSM, Eur. Phys. J. C **83,** 60 (2023).

[106] K. Kowalska, L. Roszkowski, E. M. Sessolo, and A. J. Williams, GUT-inspired SUSY and the muon $g-2$ anomaly: Prospects for LHC 14 TeV, J. High Energy Phys. 06 (2015) 020.

[107] J. Chakrabortty, A. Choudhury, and S. Mondal, Non-universal Gaugino mass models under the lamppost of muon (g-2), J. High Energy Phys. 07 (2015) 038.

[108] A. Choudhury and S. Mondal, Revisiting the exclusion limits from direct chargino-neutralino production at the LHC, Phys. Rev. D **94,** 055024 (2016).

[109] J. Dutta, P. Konar, S. Mondal, B. Mukhopadhyaya, and S. K. Rai, A revisit to a compressed supersymmetric spectrum with 125 GeV Higgs, J. High Energy Phys. 01 (2016) 051.

[110] J. Dutta, P. Konar, S. Mondal, B. Mukhopadhyaya, and S. K. Rai, Search for a compressed supersymmetric spectrum with a light Gravitino, J. High Energy Phys. 09 (2017) 026.

[111] R. K. Barman, B. Bhattacherjee, A. Chakraborty, and A. Choudhury, Study of MSSM heavy Higgs bosons decaying into charginos and neutralinos, Phys. Rev. D **94,** 075013 (2016).

[112] G. Aad et al. (ATLAS Collaboration), Search for supersymmetry in events with four or more charged leptons in 139 fb^{-1} of $\sqrt{s} = 13$ TeV pp collisions with the ATLAS detector, J. High Energy Phys. 07 (2021) 167.

[113] D. Alvestad, N. Fomin, J. Kersten, S. Maeland, and I. Strümke, Beyond cuts in small signal scenarios: Enhanced sneutrino detectability using machine learning, Eur. Phys. J. C **83,** 379 (2023).

[114] B. Bhattacherjee, C. Bose, A. Chakraborty, and R. Sengupta, Boosted top tagging and its interpretation using Shapley values, arXiv:2212.11606.

[115] E. Arganda, X. Marcano, V. M. Lozano, A. D. Medina, A. D. Perez, M. Szewc, and A. Szynkman, A method for approximating optimal statistical significances with machine-learned likelihoods, Eur. Phys. J. C **82,** 993 (2022).

[116] A. Chakraborty, S. Dasmahapatra, H. Day-Hall, B. Ford, S. Jain, and S. Moretti, Fat b-jet analyses using old and new clustering algorithms in new Higgs boson searches at the LHC, Eur. Phys. J. C **83,** 347 (2023).

[117] S. Badger et al., Machine learning and LHC event generation, SciPost Phys. **14,** 079 (2023).

[118] A. S. Cornell, W. Doorsamy, B. Fuks, G. Harmsen, and L. Mason, Boosted decision trees in the era of new physics: A smuon analysis case study, J. High Energy Phys. 04 (2022) 015.

[119] Y. Coadou, Boosted decision trees, arXiv:2206.09645.

[120] T. Chen and C. Guestrin, XGBoost: A scalable tree boosting system, arXiv:1603.02754.

[121] G. Aad et al. (ATLAS Collaboration), Search for supersymmetry in events with four or more leptons in $\sqrt{s} = 8$ TeV pp collisions with the ATLAS detector, Phys. Rev. D **90,** 052001 (2014).

[122] J. Alwall, R. Frederix, S. Frixione, V. Hirschi, F. Maltoni, O. Mattelaer, H.-S. Shao, T. Stelzer, P. Torrielli, and M. Zaro, The automated computation of tree-level and next-to-leading order differential cross sections, and their matching to parton shower simulations, J. High Energy Phys. 07 (2014) 079.

[123] T. Sjostrand, S. Mrenna, and P. Z. Skands, PYTHIA 6.4 physics and manual, J. High Energy Phys. 05 (2006) 026.

[124] B. Fuks, M. Klasen, D. R. Lamprea, and M. Rothering, Precision predictions for electroweak superpartner production at hadron colliders with Resummino, Eur. Phys. J. C **73,** 2480 (2013).

[125] J. de Favereau, C. Delaere, P. Demin, A. Giammanco, V. Lemaître, A. Mertens, and M. Selvaggi (DELPHES 3 Collaboration), DELPHES 3, A modular framework for fast simulation of a generic collider experiment, J. High Energy Phys. 02 (2014) 057.

[126] M. Cacciari, G. P. Salam, and G. Soyez, The anti-k_t jet clustering algorithm, J. High Energy Phys. 04 (2008) 063.

[127] M. Cacciari, G. P. Salam, and G. Soyez, user manual, Eur. Phys. J. C **72,** 1896 (2012).

[128] G. Aad et al. (ATLAS Collaboration), Electron and photon performance measurements with the ATLAS detector using the 2015–2017 LHC proton-proton collision data, J. Instrum. **14,** P12006 (2019).

[129] G. Aad et al. (ATLAS Collaboration), Muon reconstruction and identification efficiency in ATLAS using the full Run 2 pp collision data set at $\sqrt{s} = 13$ TeV, Eur. Phys. J. C **81,** 578 (2021).

[130] XGBoost parameters, https://xgboost.readthedocs.io/en/stable/parameter.html.

[131] S. M. Lundberg and S. Lee, A unified approach to interpreting model predictions, CoRR abs/1705.07874 (2017).

[132] L. S. Shapley, 17. A Value for n-Person Games (Princeton University Press, Princeton, NJ, 1953), pp. 307–318, 10.1515/9781400881970-018.

[133] S. M. Lundberg, G. G. Erion, and S. Lee, Consistent individualized feature attribution for tree ensembles, arXiv:1802.03888.

[134] C. Grojean, A. Paul, and Z. Qian, Resurrecting $b\bar{b}h$ with kinematic shapes, J. High Energy Phys. 04 (2021) 139.

[135] F. Cascioli, T. Gehrmann, M. Grazzini, S. Kallweit, P. Maierhöfer, A. von Manteuffel, S. Pozzorini, D. Rathlev, L. Tancredi, and E. Weihs, ZZ production at hadron colliders in NNLO QCD, Phys. Lett. B **735**, 311 (2014).

[136] P. Azzi *et al.*, Report from working group 1: Standard model physics at the HL-LHC and HE-LHC, CERN Yellow Rep. Monogr. **7**, 1 (2019).

[137] T. Binoth, G. Ossola, C. G. Papadopoulos, and R. Pittau, NLO QCD corrections to tri-boson production, J. High Energy Phys. 06 (2008) 082.

[138] SM Higgs production cross sections at $\sqrt{s} = 13$, 14 and 27 TeV (update in cern hl-lhc yr 2019), https://twiki.cern .ch/twiki/bin/view/LHCPhysics/CERNHLHE2019.

[139] https://www.hepdata.net/record/ins1852821.